Polyphase deformation, dynamic metamorphism, and metasomatism of Mount Everest's summit limestone, east central Himalaya, Nepal/Tibet

Travis L. Corthouts, David R. Lageson, and Colin A. Shaw
EARTH SCIENCE DEPARTMENT, MONTANA STATE UNIVERSITY, BOZEMAN, MONTANA 59715, USA

ABSTRACT

New samples collected from a transect across the summit limestone of Mount Everest (Qomolangma Formation) show that multiple distinct deformational events are discretely partitioned across this formation. Samples from the highest exposures of the Qomolangma Formation (Everest summit) preserve a well-developed mylonitic foliation and microstructures consistent with deformation temperatures of ≥250 °C. Thermochronologic and microstructural results indicate these fabrics were ingrained during initial contractile phases of Himalayan orogenesis, when crustal thickening was accommodated by folding and thrusting of the Tethyan Sedimentary Sequence. In contrast, samples from near the base of the Qomolangma Formation (South Summit) preserve extensional shear deformation, indicate metasomatism at temperatures of ~500 °C, and contain a synkinematic secondary mineral assemblage of muscovite + chlorite + biotite + tourmaline + rutile. Shear fabrics preserved in South Summit samples are associated with activity on the Qomolangma detachment, while the crystallization of secondary phases was the result of reactions between the limestone protolith and a volatile, boron-rich fluid that infiltrated the base of the Qomolangma Formation, resulting in metasomatism. The $^{40}Ar/^{39}Ar$ dating of synkinematic muscovite indicates the secondary assemblage crystallized at ca. 28 Ma and that shear fabrics were ingrained at ≥18 Ma. This paper presents the first evidence that Everest's summit limestone records multiple phases of deformation associated with discrete stages in Himalayan orogenesis, and that the structurally highest strand of the South Tibetan detachment on Everest was initially active as a distributed shear zone before it manifested as a discrete brittle detachment at the base of the Qomolangma Formation.

LITHOSPHERE; v. 8; no. 1; p. 38–57; GSA Data Repository Item 2015349 | Published online 16 November 2015 doi:10.1130/L473.1

INTRODUCTION

The upper summit pyramid of Mount Everest is cut by the Qomolangma detachment (Fig. 1), a splay of an orogen-scale network of low-angle normal faults known as the South Tibetan detachment (Burchfiel et al., 1992). On Everest, the hanging wall of the Qomolangma detachment is composed of the Qomolangma Formation (Figs. 2A–2C), an Ordovician limestone deposited along the passive northern margin of India (Yin and Kuo, 1978; Torsvik et al., 2009; Harper et al., 2011), which now forms the upper summit pyramid of Mount Everest, above the famed Yellow Band (Myrow et al., 2009).

Everest has long been referred to by Tibetans as Qomolangma, and the rock formation that caps this natural pyramid preserves this name. There have been many investigations on the structural, metamorphic, and magmatic evolution of the Mount Everest massif (e.g., Odell, 1925, 1967; Gysin and Lombard, 1959, 1960; Gansser, 1964; Burchfiel et al., 1992; Lombardo et al., 1993; Pognante and Benna, 1993; Searle, 1999a, 2003; Carosi et al., 1999; Simpson et al., 2000; Searle et al., 2003; Sakai et al., 2005; Law et al., 2004, 2011; Jessup et al., 2006, 2008; Myrow et al., 2009; Streule et al., 2012). However, the extreme terrain and high-altitude exposure of the Qomolangma Formation have hindered geologists from directly studying or sampling this formation, and most characterizations have been based on "grab samples" collected from the summit of Everest (e.g., Gysin and Lombard, 1959, 1960; Gansser, 1964; Searle et al., 2003; Sakai et al., 2005; Jessup et al., 2006). This investigation is based on a suite of new samples collected from a transect across the Qomolangma Formation, on the southeast ridge of Everest, including 11 samples from six different locations between the summit of Everest and the South Summit, the latter at ~15 m above the Qomolangma detachment (Table 1; Fig. 2A).

We have documented variations in fabric, mineralogy, and microstructure across the Qomolangma Formation, complemented by calculations of flow stress and deformation temperatures using Ti-in-biotite, Ti-in-quartz (TitaniQ), and microstructure-based geothermometry. A feature of considerable interest is the secondary mineral assemblage found in samples collected at the base of the Qomolangma Formation (South Summit). The secondary paragenesis coupled with geochemical analysis of tourmaline provide insight into the conditions of crystallization and the origin of the extrinsic fluids involved. We used $^{40}Ar/^{39}Ar$ dating of synkinematic muscovite to constrain the age of metasomatism and motion on the Qomolangma detachment. These data provide new information about the style and timing of detachment faulting in the Everest region, the metasomatic envelope of Himalayan metamorphism, and the influence that fluids may have had on faulting in the South Tibetan detachment.

GEOLOGIC BACKGROUND

Everest Region Structural Setting

The Qomolangma Formation (also referred to as the "summit limestone") is a sequence of gray-green limestone that comprises the uppermost ~125 m of Mount Everest (Figs. 1 and 2). This package of rock is part of the Tethyan Sedimentary Sequence, a lithotectonic unit of folded and faulted sedimentary and metasedimentary rocks exposed continuously for more than 2000 km along the length of the Himalayan orogen

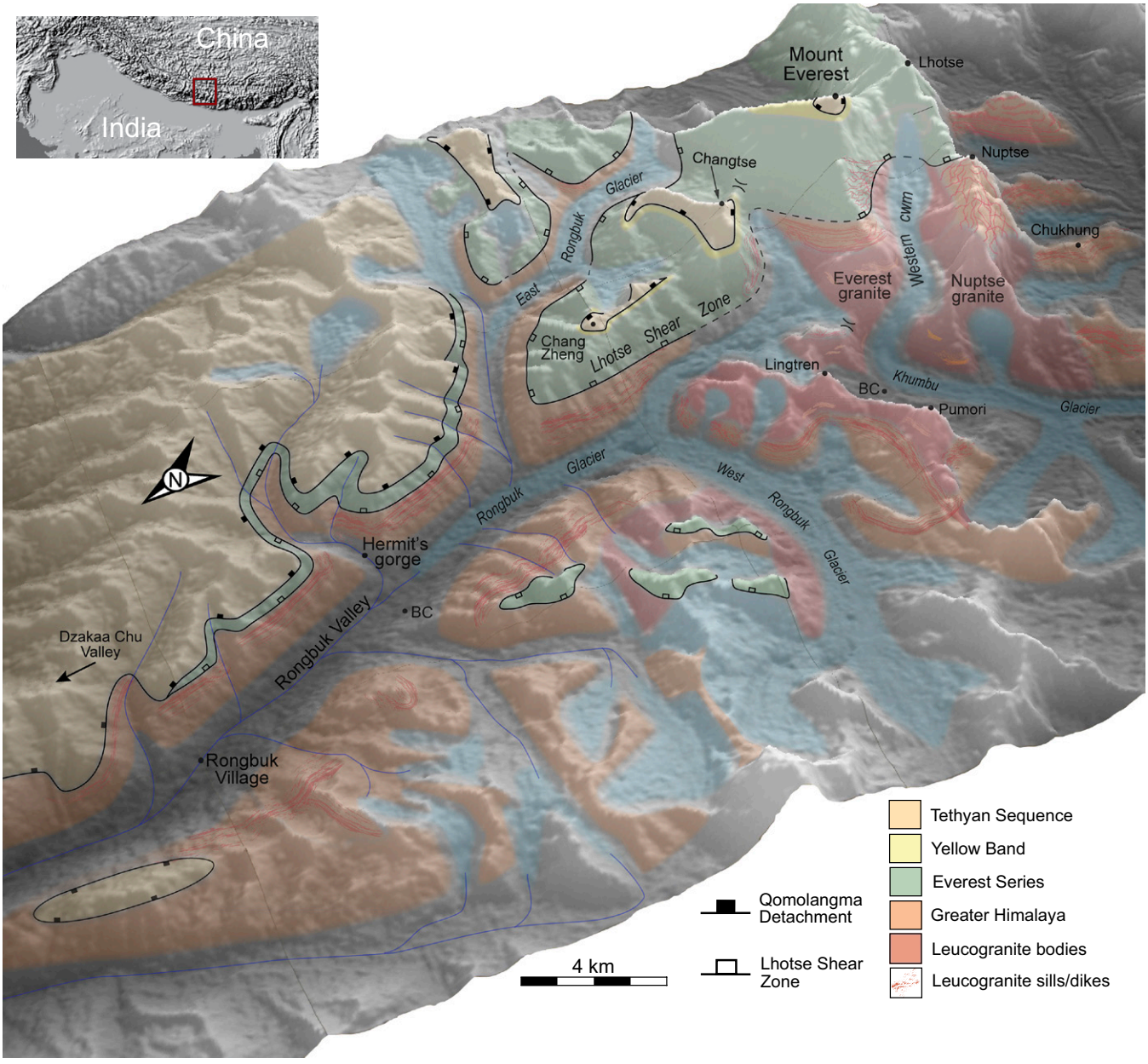

Figure 1. Simplified geologic map of the Everest area adopted from Carosi et al. (1998), Searle, (2003), and Jessup et al. (2008). Modifications are based on field work completed during a field season in the Khumbu Glacier region, high-altitude images taken from helicopter by Simone Moro and Max Lowe, Google Earth satellite imagery, and on gigapixel-resolution images viewable on Glacierworks.org. BC—Base Camp. Inset: shaded relief map of the Himalaya showing the location of the Everest region (red box).

(Garzanti, 1999; Hodges, 2000; Yin, 2006; Kellett and Godin, 2009). This sequence is bounded to the north by the Indus-Tsangpo suture zone and to the south by low-angle, north-dipping normal faults and shear zones of the South Tibetan detachment (Burchfiel et al., 1992; Hodges, 2000; Murphy and Yin, 2003). The South Tibetan detachment was first recognized in north-central Nepal by Caby et al. (1983) and was subsequently mapped in detail by Burg and Chen (1984) and Burchfiel et al. (1992) as separating passive-margin sedimentary rocks of the Tethyan Sedimentary Sequence in its hanging wall from high-grade metamorphic rocks and anatectic leucogranites of the Greater Himalayan Sequence in the footwall (Fig. 3). The South Tibetan detachment is often distinguished by superposed detachments, typically a lower detachment comprising a wide shear zone and a structurally higher and younger brittle detachment (e.g., Vannay and Hodges, 1996; Searle, 1999a; Searle and Godin, 2003; Leloup et al., 2010; Cooper et al., 2012), with the upper structure marking a significant jump in metamorphic grade.

In the Everest area, the Greater Himalayan Sequence is a 15–20-km-thick sequence of sillimanite-grade orthogneiss, migmatite, and leucogranite (Fig. 3; Searle et al., 2003, 2006) that has evolved through two widely recognized episodes of metamorphism (Hodges et al., 1988; Pêcher, 1989; Simpson et al., 2000). The earlier "Eohimalayan" event, between 39 and 32 Ma (Simpson et al., 2000; Catlos et al., 2002; Cottle

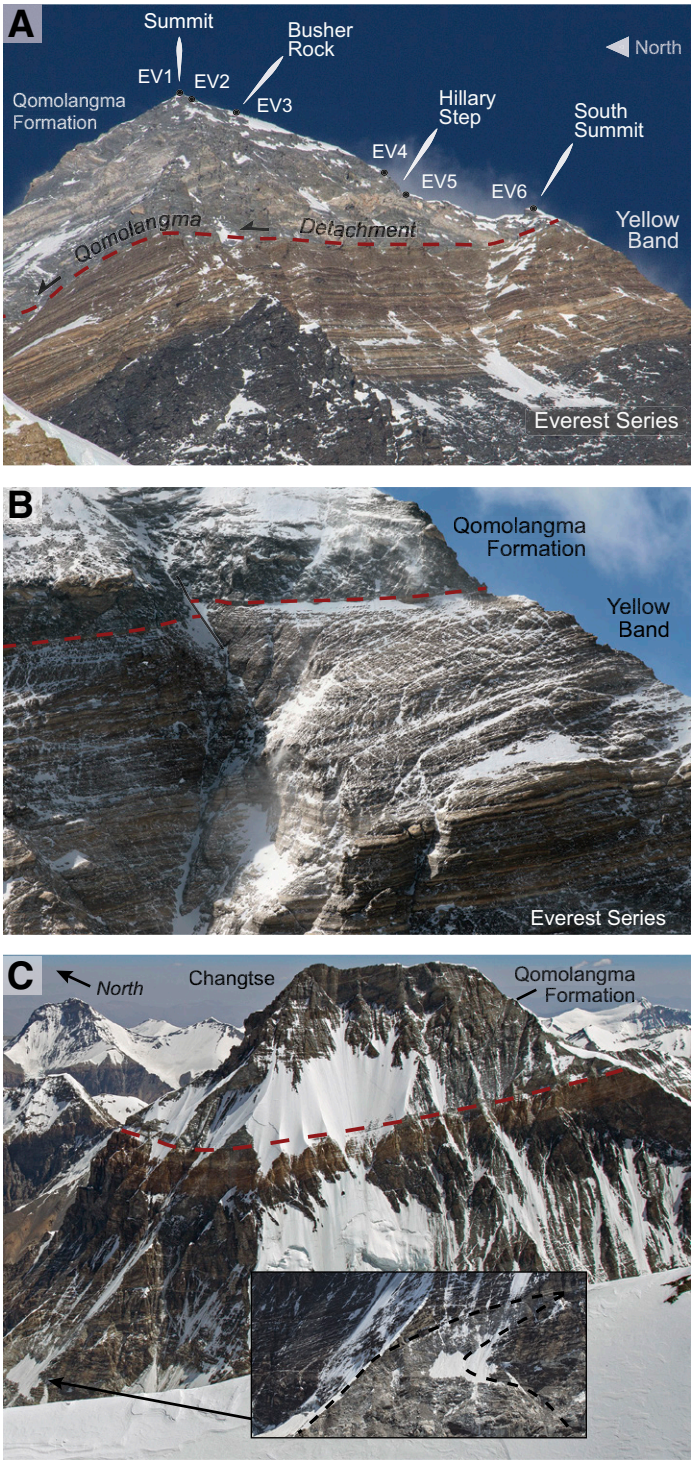

Figure 2. (A) Southwest face of Everest showing sample locations, the significant lithologic units, and the location of the Qomolangma detachment. (B) High-altitude helicopter image of the north face of Everest provided by Simone Moro showing the Qomolangma Formation, Yellow Band, and Qomolangma detachment (red dashed line). The prominent gully is the Hornbein Couloir. (C) The Qomolangma Formation and Yellow Band exposed on Changtse, immediately north of Everest. Leucogranites at the base of Changtse nearly reach the Yellow Band. Inset shows a leucogranite body that appears to be deflected to the south, against tectonic grain. Scale: The Yellow Band is 164 m thick on Everest (based on stratigraphic thickness calculations in this study).

TABLE 1. QOMOLANGMA FORMATION SAMPLES

Sample ID	Sample location	Elevation (m)	Sample weight (g)
EV1	Summit	8840	334.63
EV2a	Summit	8836	329.73
EV2b	Summit	8836	424.90
EV3a	Busher Rock	8811	237.49
EV3b	Busher Rock	8811	80.74
EV3c	Busher Rock	8811	252.26
EV4	Hillary Step—top	8783	180.62
EV5	Hillary Step—base	8764	169.67
EV6a	South Summit	8750	103.23
EV6b	South Summit	8750	290.82
EV6c	South Summit	8750	102.39

et al., 2009), was associated with initial crustal thickening and prograde Barrovian metamorphism at temperatures of 550–680 °C and pressures of 8–10 kbar (Pognante and Benna, 1993; Borghi et al., 2003). Subsequent "Neohimalayan" metamorphism, between 28 and 22.6 Ma (Simpson et al., 2000; Viskupic et al., 2005; Cottle et al., 2009), was characterized as a high-temperature, low-pressure event that recorded near-isothermal decompression to ~3 kbar at temperatures between 650 and 750 °C (Pognante and Benna, 1993; Simpson et al., 2000; Searle et al., 2003; Jessup et al., 2008). During the Neohimalayan event, vapor-absent dehydration melting of muscovite and biotite within the Greater Himalayan Sequence (Scaillet et al., 1990, 1996; Prince et al., 2001; Searle, 2013) led to the generation and emplacement of leucogranite throughout the upper structural levels of the Greater Himalayan Sequence (Fig. 3; Searle, 1999b; Searle et al., 2003, 2009).

On Mount Everest, the upper margin of the Greater Himalayan Sequence is bounded by a broad top-down-to-the-northeast ductile shear zone known as the Lhotse shear zone, which is the lower portion of the South Tibetan detachment on Everest (Figs. 1 and 3). This fault zone was first suggested by Lombardo et al. (1993), subsequently regarded by Carosi et al. (1998) as a ≥1000-m-thick shear zone, and later described by Searle (1999a) and Searle et al. (2003) as a distinct break between upper-amphibolite-facies gneiss and leucogranite of the Greater Himalayan Sequence in its footwall and middle- to upper-greenschist-facies schist and calc-silicate of the Everest Series in its hanging wall (Searle, 2003). More recent thermobarometric investigations suggest that metamorphic temperatures across this structure are near-isothermal, and that metamorphic grade in the Everest Series is gradational, from amphibolite facies at the base of the unit to upper-greenschist facies at the top (Waters et al., 2006; Jessup et al., 2008). However, due to its poor exposure, the exact nature and metamorphic significance of the Lhotse shear zone will likely remain debatable.

The top of the Everest Series is marked by the Yellow Band (Fig. 2A), a sequence of course-grained marble and schist that underlies Everest's summit pyramid and is separated from the Qomolangma Formation above by the structurally highest portion of the South Tibetan detachment, the Qomolangma detachment (Figs. 2A–2C; Gansser, 1964; Burchfiel et al., 1992; Hodges et al., 1992; Sakai, 1997; Searle, 1999a; Searle et al., 2003; Sakai et al., 2005). On Everest, the Qomolangma detachment dips between 20° and 15° northeast and, as described by Sakai et al. (2005) on the northeast ridge, is a discrete brittle fault. Traced downdip from the upper slopes of Everest, the Qomolangma detachment cuts across the underlying Everest Series and merges with the Lhotse shear zone, placing relatively unmetamorphosed Tethyan limestone and calcareous shale directly over sillimanite gneiss and leucogranites of the Greater Himalayan Sequence (Figs. 1 and 3; Burchfiel et al., 1992; Carosi et al., 1998; Searle et al., 2003).

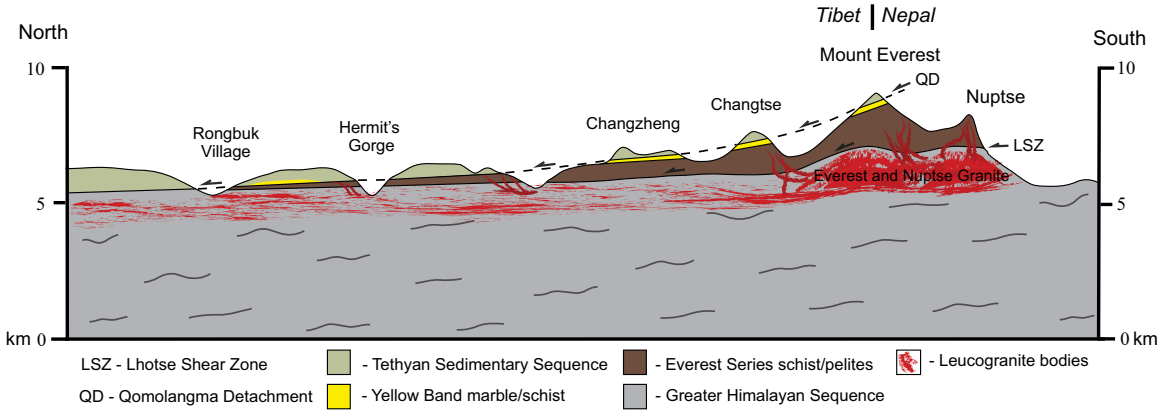

Figure 3. Generalized cross section through the Everest massif and the Rongbuk Valley to the north, modified from Searle et al. (2003), Searle, (2003), and Jessup at al. (2008).

In the Rongbuk Valley, immediately north of Everest (Fig. 1), the Qomolangma detachment dips between 3° and 10 ° and is characterized by a brittle detachment above a structurally downward sequence of marble, calc-silicate, leucogranite, and biotite-sillimanite schist/gneiss that is variably mylonitized for at least 1000 m below the detachment surface (Carosi et al., 1998; Murphy and Harrison, 1999; Searle, 2003; Jessup et al., 2006). The age of shearing and mylonitization has been partly constrained by Searle et al. (2002) at 17.0 ± 0.2 Ma, and by Searle et al. (2003) at 16.9 ± 0.2 Ma, based on U-Pb dating of monazite from mylonitic samples. Murphy and Harrison (1999) obtained similar Th-Pb ages from a mylonitic sill and a deflected leucogranite dike in the immediate footwall, which indicate ductile shearing was active at ca. 17 Ma. Using both U/Th-Pb isotope dilution–thermal ionization mass spectrometry (ID-TIMS) and laser ablation–multicollector–inductively coupled plasma–mass spectrometry (LA-MC-ICP-MS) dating of leucogranite samples collected at Hermit's Gorge (Fig. 1), Cottle et al. (2015) showed that ductile shearing in the footwall was ongoing at 16.4 Ma, but ceased prior to 15.6 Ma, and that brittle faulting is younger than 15.4 Ma. Deformation temperatures, determined by quartz *c*-axis fabric opening angles, increase linearly with depth in the footwall, from 490 °C at 10–20 m below the detachment to 680 °C at ~420 m (Law et al., 2004, 2011).

Qomolangma Formation

The first documented description of Everest's summit limestone came from a sample collected in 1933 by Lawrence Wager, who described the specimen as "gray nobbly limestone, not noticeably metamorphosed" (Lawrence Wager Collection records, Oxford University Museum; see also Wager, 1934). Subsequent descriptions of the Qomolangma Formation were made by Gysin and Lombard (1959, 1960) and Augusto Gansser (1964), using samples gathered by the successful Swiss and American expeditions of 1956 and 1963, respectively (see also Odell, 1967). Professor Gansser described the various summit samples as being lithologically identical and composed of thin-bedded, fine-grained calc-schist or platy limestone with crinoid fragments that stand out against the "finer-grained calcites of the groundmass" (Gansser, 1964, p. 158–164). Burchfiel et al. (1992) described samples collected from the summit of Everest by a Bulgarian climber in 1984 as limestones with a weakly developed solution cleavage and inferred that they were similar to Tethyan rocks exposed in the Qomolangma detachment hanging wall in the Rongbuk Valley.

More recent descriptions of Everest's summit limestone have been provided by Searle et al. (2003), Sakai et al. (2005), and Jessup et al. (2006). They summarized the formation as thick-bedded, relatively unmetamorphosed, impure limestone containing calcite porphyroclasts within a fine-grained matrix of either micrite (Sakai et al., 2005) or recrystallized calcite (Jessup et al., 2006). Searle et al. (2003) reported samples collected close to the summit to have fragments of conodonts and corals, and one sample contained 88% calcite, 9% dolomite, 2% quartz, and 1% illite/muscovite, had a preferred alignment of calcite grains into a strong foliation, contained calcite porphyroclasts with deformation twins, and had strain-free detrital quartz grains. In comparison, samples collected 6 m below the summit of Everest by Sakai et al. (2005) contained abundant fragments of crinoids, trilobites, ostracods, and brachiopods and were seemingly much less sheared and recrystallized. Jessup et al. (2006) noted undulose extinction in some detrital quartz, as well as other strain-free grains within the calcite matrix, and these authors as well as Searle et al. (2003) suggested deformation temperatures of <200–250 °C. The uplift history of the Qomolangma Formation is constrained by apatite fission-track data from a single summit sample, which suggests the formation cooled below ~130 °C by 30.5 ± 5.1 Ma (Streule et al., 2012). This was interpreted by these authors as evidence for exhumation of the summit limestone in the Oligocene, during initial Eohimalayan crustal thickening and uplift.

METHODS

Detailed analytical conditions for electron microprobe analyses and electron backscattered diffraction (EBSD) analyses are given in GSA Data Repository Appendix 1.[1] Descriptions of fabrics are reported from thin sections cut normal to the foliation and parallel to the lineation. Grain-size data for quartz and calcite were acquired automatically using EBSD analysis and manually using the line intercept method. To ensure high-quality results from electron microprobe and EBSD analyses, and to allow easier optical recognition of intragranular strain features, 30 µm thin sections were repolished in three stages, using: (1) 3 µm diamond suspension polish for 20 min; (2) 1 µm diamond suspension polish for 20 min; and (3) 0.05 µm colloidal silica suspension polish for 8 h.

The $^{40}Ar/^{39}Ar$ dating of muscovite was carried out at the U.S. Geological Survey (USGS) $^{40}Ar/^{39}Ar$ Laboratory in Denver, Colorado, by USGS

[1]GSA Data Repository Item 2015349, Appendices 1–3, is available at www.geosociety.org/pubs/ft2015.htm, or on request from editing@geosociety.org.

research geologist Michael Cosca. Irradiation of the sample material was done in a nuclear reactor, followed by incremental heating of the sample with an infrared (CO_2) laser, and isotopic measurement of argon with a Mass Analyzer Products (MAP) 215–50 mass spectrometer.

QOMOLANGMA FORMATION SAMPLES

Eleven nonoriented samples were collected from six locations across the southeast ridge of Everest by Nepali Sherpa climbers trained and equipped by the authors for geologic sampling (Table 1; Fig. 2A). These samples have been divided into three structural horizons: summit samples (EV1 and EV2a–EV2c), Hillary Step samples (EV4 and EV5), and South Summit samples (EV6a–EV6c).

Summit Samples

Three samples (EV1, EV2a, and EV2b) were collected from exposed outcrops in the immediate vicinity of Mount Everest's summit (Fig. 2A). Sample EV1 is the highest-elevation sample, collected from the uppermost exposed outcrop on the southwestern aspect of the summit, while samples EV2a and EV2b were collected closer to the southeast ridge and a few meters lower than EV1. Three additional samples (EV3a–EV3c), grouped with summit samples, were collected further down the ridge at an outcrop referred to as "Busher Rock" by our Sherpa team (Fig. 2A).

Sample Description

All summit samples are lithologically identical and contain the common mineral assemblage calcite + quartz + dolomite + white mica ± pyrite ± zircon. Calcite has undergone significant grain-size reduction via dynamic recrystallization, resulting in a matrix of fine-grained, elongate, and strain-free calcite grains with an average grain size and aspect ratio of 8.3 μm and 2.0, respectively. Alignment of elongate calcite grains forms a grain shape preferred orientation fabric, which is deflected around calcite porphyroclasts, creating calcite augen and a well-developed mylonitic foliation in all summit samples (Figs. 4A–4B). The extensive recrystallization of calcite and development of tectonic stylolites have largely destroyed the primary fabric. The only vestiges of primary constituents are some calcite porphyroclasts that can be recognized as fossil fragments, most abundant of which are crinoid ossicles (Fig. 4A). Laths of white mica up to 250 μm in length are dispersed throughout the matrix and are generally parallel to fabric. Large pyrite grains up to 800 μm, interpreted to be of diagenetic origin, are present along with trace amounts of small detrital zircon grains averaging ~20 μm.

Porphyroclastic grains of calcite between 250 and 1500 μm in diameter are characterized by subgrain development and type IV deformation twins (Fig. 4C), indicating deformation temperatures of >250 °C (Burkhard, 1993; Ferrill et al., 2004). Subgrains in porphyroclasts are similar in size to the recrystallized grains in the matrix (Fig. 4C), suggesting that recrystallization was accommodated through subgrain rotation (Passchier and Trouw, 2005). Several studies on naturally deformed marble and limestone show that the onset of dynamic recrystallization in calcite coincides with metamorphic temperatures between 250 °C and 350 °C (e.g., Burkhard, 1993; Ferrill and Groshong, 1993; Evans and Dunne, 1991). Based on the observed microstructures and the proportion of recrystallized matrix, summit samples are classified as calc-mesomylonites (Passchier and Trouw, 2005).

Detrital quartz grains are scattered throughout the matrix and are equant to elongate, subangular to subrounded, and range in size between 25 μm and 125 μm. Some detrital quartz grains have patchy or sweeping undulose extinction. Optical cathodoluminescence (CL) images of these detrital grains do not show overgrowths or any evidence of static growth, although most quartz grains luminesce blue, indicating elevated concentrations of trace Ti (Rusk et al., 2006).

Dolomite, revealed by alizarin red-S stain, exists as unimodal aggregates of nonplanar (xenotopic) dolomite (Gregg and Sibley, 1984; Sibley and Gregg, 1987) and as solitary grains of saddle dolomite (Radke and Mathis, 1980). Aggregates of dolomite overprint foliation and, thus, formed postdeformation. Saddle dolomite grains are characteristically similar to those described by Radke and Mathis (1980), having curved crystal faces and sweeping extinction. These grains deflect the matrix flow fabric and, therefore, would have formed prior to deformation.

Busher Rock samples are quite similar to summit samples, containing a continuous foliation defined by the alignment of elongate calcite grains, white mica, and, to a lesser degree, fabric-parallel veins. However, there are no residual calcite porphyroclasts or fossil fragments in these samples, and the texture of these rocks has progressed to ultramylonite. Another important difference in Busher Rock samples is the presence of diffuse bands of insoluble material, thought to have been burial stylolites, which have been tightly folded by ductile shearing in the matrix (Fig. 4E). The axial surfaces of these folds are parallel to foliation, indicating that foliation and folds are genetically related (Passchier and Trouw, 2005). Folding of primary layering (S_0) during foliation development (S_1) can be related to shear zone development, which generally occurs in calcite at temperatures ~275 °C (Schenk et al., 2005). Also, a veinlike aggregate of quartz with sweeping and patchy undulose extinction suggests deformation temperatures of ~280 °C (Fig. 4D; Stipp et al., 2002a).

Flow Stress Calculation

The grain size of dynamically recrystallized calcite has been used to calculate flow stress using the methods and constants of Rutter (1995) for subgrain rotation recrystallization. Grain size data yield an average recrystallized grain size of 8.3 ± 3.8 μm, which corresponds to a flow stress of ~126 MPa. The accuracy of this measurement is largely dependent on the assumption that the apparent grain size is solely a function of dynamic recrystallization (dislocation creep). It is possible that other deformation processes did in fact occur during and following dislocation creep, although CL images do not show any sign of static grain growth. Therefore, the observable grain size in thin section is assumed to be greater than or equal to that immediately following dynamic recrystallization, and flow stress calculations for summit samples are taken as minimum estimates.

Hillary Step Samples

The Hillary Step, at 8770 m on the southeast ridge, is a steep, ~20-m-high cliff that crops out nearly halfway between the summit of Everest and the bottom of the Qomolangma Formation (Fig. 2A). Two samples were collected at the Hillary Step, one from the top of the step (EV4) and one from immediately below the step (EV5; Table 1).

Sample Description

Hillary Step samples are identical to each other in terms of lithology and microstructure, and they are composed of the mineral assemblage calcite + quartz + white mica + albite ± dolomite ± zircon. Calcite has undergone extensive deformation, and all original calcite grains have been consumed by recrystallization, such that relict porphyroclasts and fossil fragments are absent (Figs. 5A–5B). Detrital quartz grains are scattered throughout the matrix of each sample much in the same way as summit samples and are generally subangular to subrounded, range between 40 and 200 μm in diameter, and have the same blue luminescence under CL. Foliation-parallel white mica laths up to ~300 μm in length with well-

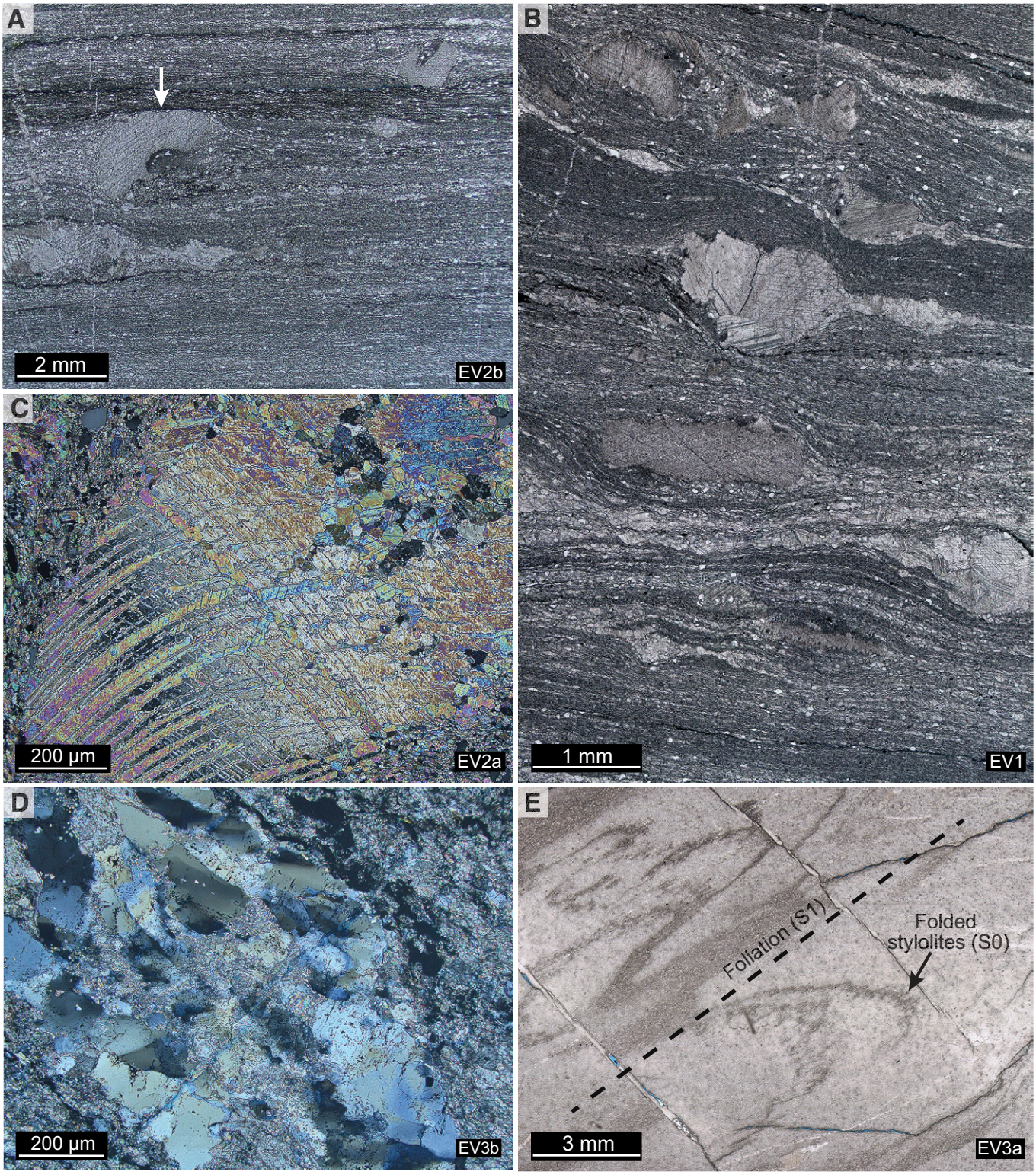

Figure 4. Photomicrographs of summit samples. (A) Relict crinoid ossicle fragment (arrow) in a matrix of fine-grained recrystallized calcite. (B) Well-developed mylonitic foliation seen throughout summit samples. (C) Calcite porphyroclast with serrated twin boundaries due to twin boundary migration (type IV deformation twins; Burkhard, 1993). Notice the newly recrystallized grains at the top right of the clast, which are similar in size to recrystallized grains in the matrix. (D) A veinlike aggregate of quartz with sweeping and patchy undulose extinction. (E) Folded diagenetic stylolites with the axial plane of folds parallel to foliation. A, B, and E are in plane polarized light.

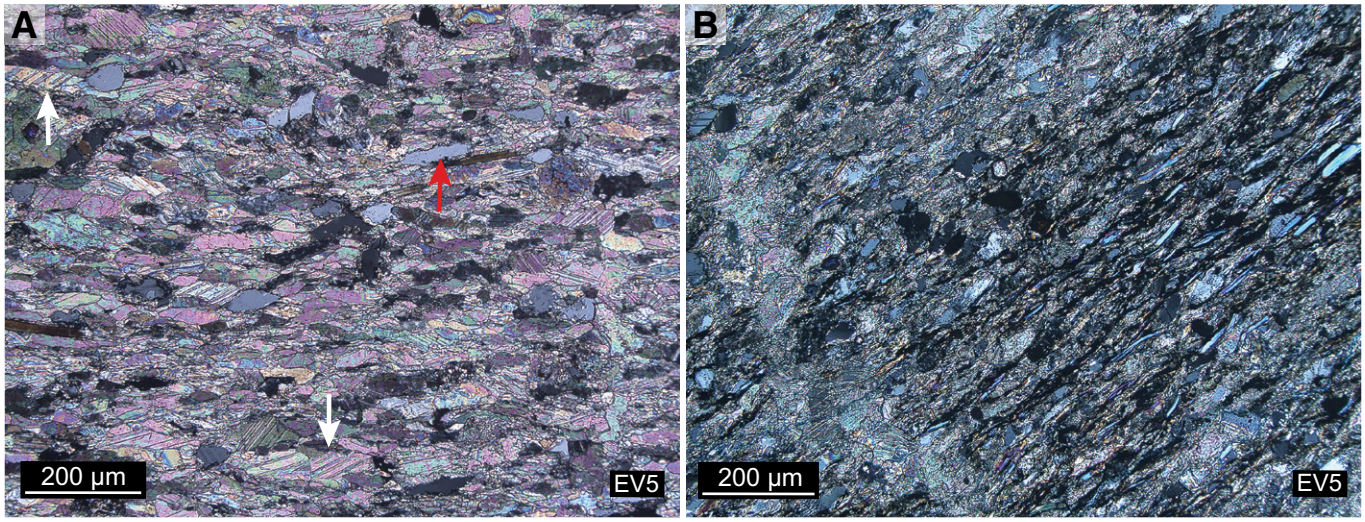

Figure 5. Photomicrographs of Hillary Step samples. (A) Elongate calcite and detrital quartz grains define a continuous foliation in Hillary Step samples. White arrows point to larger-than-average twinned calcite grains; red arrow points to an elongate detrital quartz grain typical of Hillary Step samples. (B) Evidence for dissolution of calcite and for significant diffusive mass transfer is seen as zones of concentrated insoluble residue with abundant aligned white mica laths.

defined grain boundaries are scattered throughout each sample. Detrital grains of twinned albite and zircon were observed in some thin sections as well as sparse fabric-parallel grains of dolomite.

Matrix calcite grains are elongate with an average grain size and aspect ratio of 21.1 ± 12.8 µm and 2.8 ± 1.2 respectively. Relative to summit samples, the increased aspect ratio of calcite at the Hillary Step has amplified the grain shape preferred orientation fabric, and the alignment of elongate calcite, quartz, and white mica defines a continuous foliation (Fig. 5A). Amongst the generally strain-free recrystallized matrix, there is a population of calcite grains of larger relative size (~40–60 µm) that commonly have consistently oriented thin rational twins (Fig. 5A). CL images do not show evidence that larger grains have grown statically, and it is unclear how two different grain-size populations evolved alongside each other.

Sample EV5 contains a significant amount of insoluble material that is concentrated into an ~1-cm-thick band composed of smooth seams of opaque residue that define a domainal spaced cleavage (Fig. 5B; Passchier and Trouw, 2005). Aligned white mica laths are abundant within cleavage domains, and their straight, euhedral grain boundaries suggest that they crystallized syndeformation, rather than being of detrital origin. Some seams within the dark band have been isoclinally folded and, though attenuation of their limbs makes it difficult to confirm, appear to connect into a thin-section–scale z fold.

South Summit Samples

The South Summit at 8750 m is a topographic prominence on the southeast ridge (Fig. 2A). In terms of its geologic significance, it marks the lower limit of our sampling transect across the Qomolangma Formation, at ~15 m above the Qomolangma detachment. Three samples (EV6a–EV6c) were collected from accessible outcrops exposed on the west side of the ridge (Table 1). An important difference from structurally higher samples is that two of the three samples contain large deformed quartz veins (Figs. 6 and 7); sample EV6a is composed entirely of a quartz vein, ~4 cm thick, that is bounded between green micaceous layers, while sample EV6b is a well-foliated specimen with an ~2-cm-thick, foliation-parallel quartz vein that divides the sample in half.

Sample Description

South Summit samples do not have any discernible depositional fabric or relict calcite porphyroclasts, nor are there any fossil fragments. There is consistent evidence of foliation-parallel extensional strain throughout all samples, seen by boudinage of the large quartz vein in EV6b (Fig. 6A) and by microboudinage of individual tourmaline grains (Fig. 7F). In sample EV6b, foliation is defined by the alignment of elongate calcite grains and white mica (Fig. 6B), and by differentiation of linear calcite aggregates and domains of insoluble residue (Figs. 6A and 6F). This foliation is deflected around the quartz vein or large fragments that have broken from the vein, producing a mylonitic foliation (Fig. 6A). Based on the different fabric elements, sample EV6b is considered to be a marble mylonite. In contrast, foliation in EV6c is defined by aligned muscovite throughout the sample, seams of insoluble residue, and lenses of quartz; this sample is considered a calc-silicate or calc-schist.

The composition of South Summit samples is quite different from structurally higher samples, containing a bulk assemblage of calcite + quartz + white mica + chlorite + biotite + tourmaline + rutile ± microcline ± dolomite. This mineralogy is described in terms of phases that are relicts of the limestone protolith (primary phases), and minerals that crystallized from reactions between primary phases and hydrothermal fluids (secondary phases).

Primary mineral assemblage. Primary phases consist of calcite + quartz + white mica ± zircon (detrital), and together these phases comprise what is considered to be the matrix in South Summit samples. Quartz occurs as large veins (Figs. 6A and 7A) and as 25–150 µm, subrounded to rounded grains scattered throughout the matrix. CL images of matrix quartz grains show core-overgrowth structures, and fluid inclusions often outline the former grain boundary, indicating static grain growth. Calcite shows a range of fabrics, microstructures, and grain sizes. Throughout much of the matrix, calcite is significantly deformed, and grains are slightly elongate and have serrated boundaries, rational or irrational deformation twins, and variable grain size between 20 and 250 µm (Figs. 6B and 6F). In many grains with deformation twins, there is evidence of twin boundary migration, as twins are often serrated and irregular in nature or have nearly replaced the whole grain (Fig. 6F). In the stress shadows

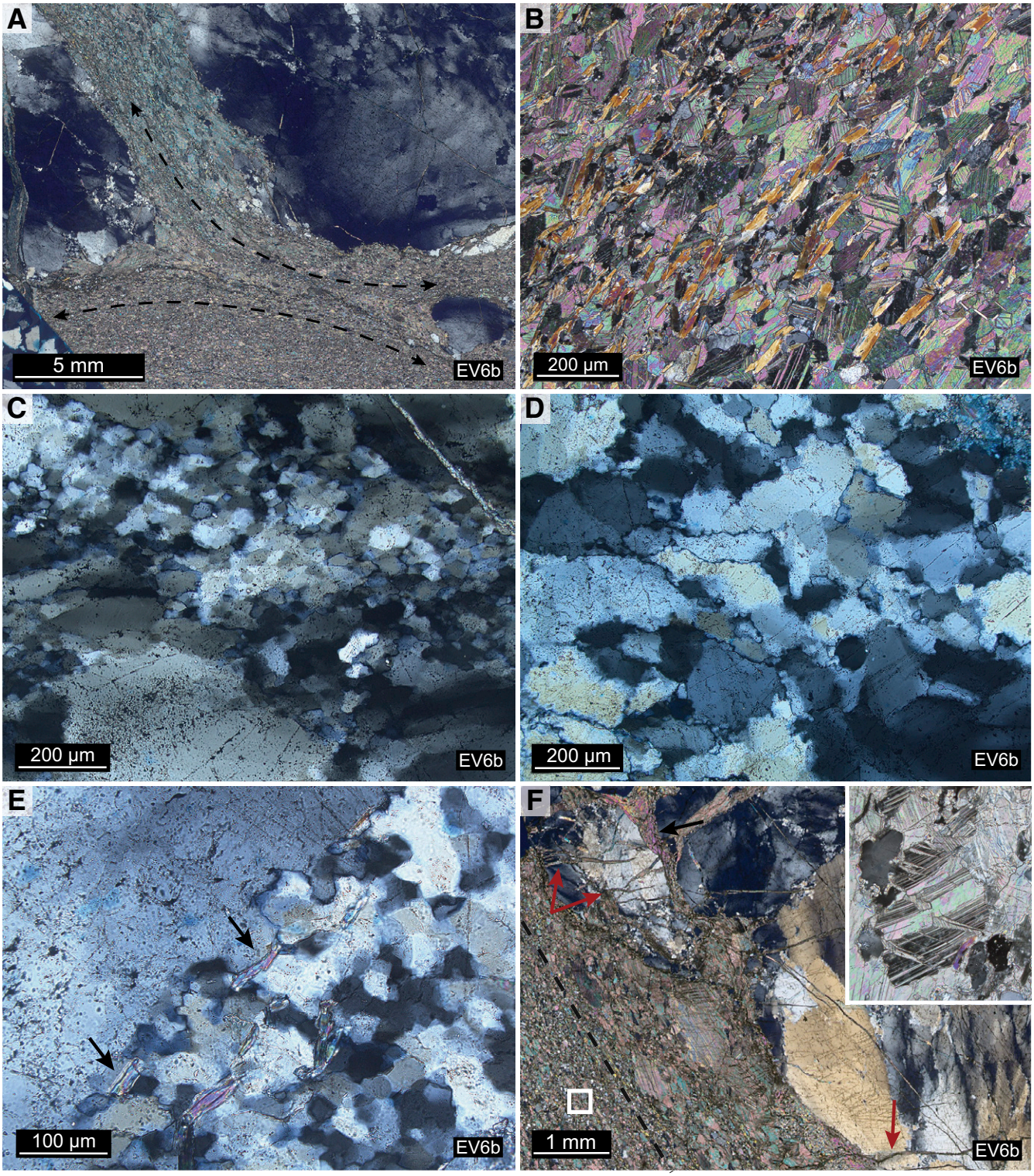

Figure 6. Photomicrographs of South Summit samples. (A) Boudinage of the large quartz vein in EV6b. Dashed lines parallel foliation and outline the "necked" region of boudinage. (B) Matrix of coarse-grained, twinned calcite and abundant aligned neocrystallized muscovite grains (yellow-orange mica laths). (C) Zone of subgrain rotation recrystallization within the EV6b quartz vein. (D) Zone of grain boundary migration recrystallization with the EV6b quartz vein. (E) Pinning of grain boundaries by white mica laths (arrows). (F) Different generations of fractures in South Summit samples. Generation-one fractures (black arrow) have a random orientation and are filled with secondary phases, whereas generation-two fractures (red arrows) are consistently oriented subperpendicular to the foliation (dotted line) and may crosscut the vein, aggregates of secondary phases, and foliation. Inset at top right is a higher-magnification image of a typical calcite grain in the matrix; inset width = 300 µm.

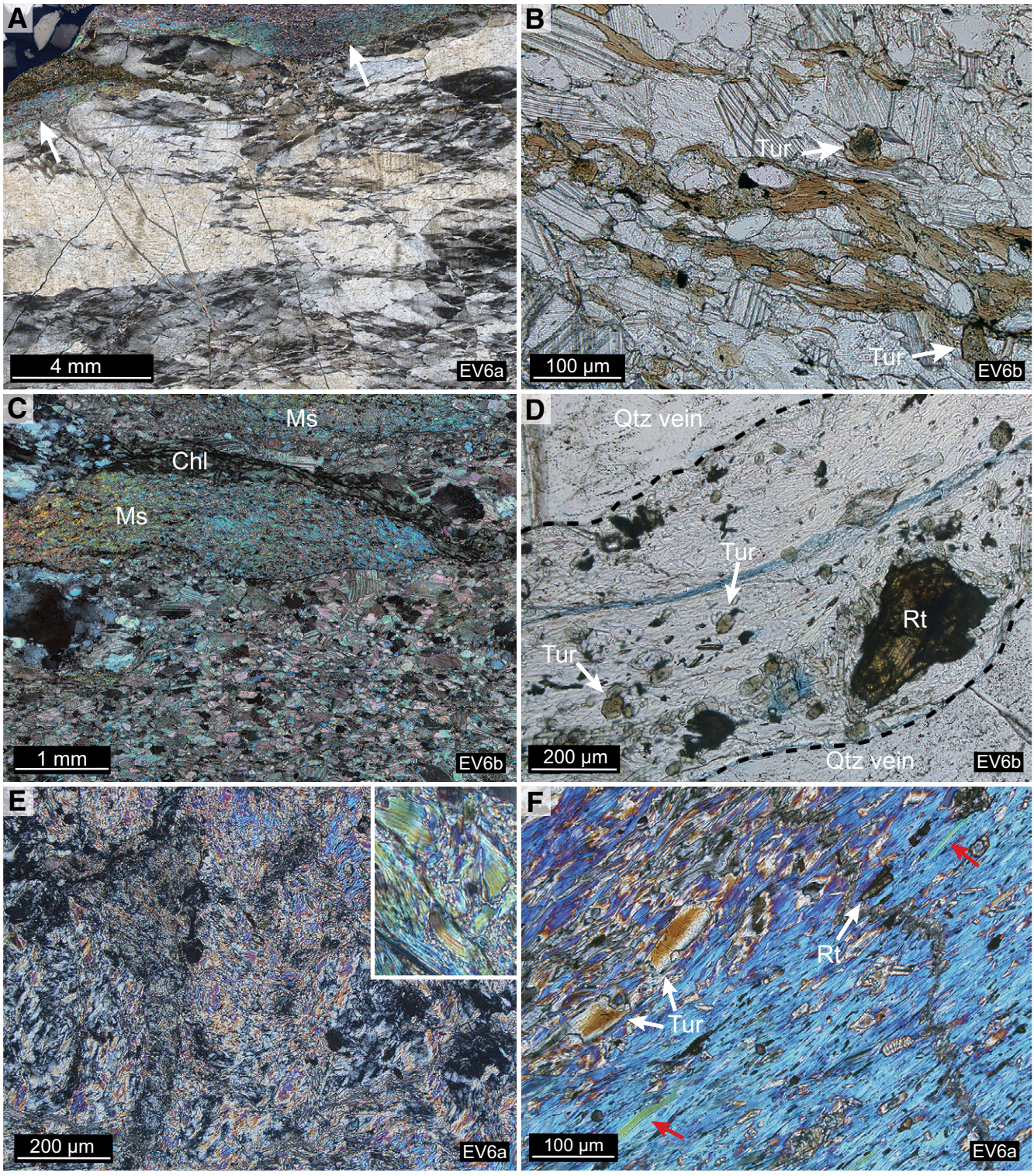

Figure 7. Photomicrographs of South Summit samples; (A) Thin-section scan of EV6a showing the deformed quartz vein with prismatic subgrains. Arrows point to a large aggregate of secondary phases along the vein edge from which muscovite was extracted for $^{40}Ar/^{39}Ar$ dating. (B) Secondary biotite (cinnamon grains) and tourmaline (Tur) occurring within the matrix nearby to large aggregates of other secondary phases. (C) Elongate, foliation-parallel aggregates of secondary phases in the matrix of EV6b; the dark-green portion is chlorite (Chl) surrounded by muscovite (Ms). Tourmaline and rutile also occur within these aggregates. (D) A generation-one fracture in the large quartz (Qtz) vein in EV6b filled by secondary phases. The image was taken in plane polarized light to better reveal tourmaline (Tur) and rutile (Rt); clear muscovite fills the space between these grains. (E) Aggregate of deformed and partly recrystallized muscovite grains in population one. Inset at top right is a higher-magnification view of bent, population-one muscovite grains; inset width = 300 µm. (F) Scaly aggregate of muscovite with a few well-defined, undeformed neocrystallized muscovite grains in population two (red arrows). Fine-grained rutile (Rt) and a boudinaged tourmaline (Tur) grain are also present. B and D are plane polarized light.

formed around asperities of the large quartz vein in sample EV6b, calcite often forms zones of subhedral to euhedral, rationally twinned, interlocking grains generally between 100 and 600 µm in diameter (Fig. 6F). CL images of these grains show equidimensional core overgrowths that lead into well-defined grain boundaries, again indicating static grain growth. In some zones of interlocking coarse calcite, grains are anhedral and have interfingering grain boundaries, suggesting grain boundary migration recrystallization (e.g., Schmid et al., 1980, their Fig. 12).

The deformed quartz veins in EV6a and EV6b have large prismatic subgrains (Fig. 7A), subdomains with sweeping undulose extinction (Fig. 6A), and domains of dynamically recrystallized grains that display fabrics indicative of both subgrain rotation and grain boundary migration (Figs. 6C–6E). Thin section scans show that recrystallization is more pervasive for the EV6a vein, occupying 60%–80% of the total vein. Recrystallization is more heterogeneous across the EV6b vein, occupying zones that account for 30%–40% of the vein. Recrystallized grains formed by subgrain rotation are equant, range between 25 and 35 µm in diameter, and are usually arranged as elongate bands (Fig. 6C). Areas of grain boundary migration recrystallization are volumetrically more abundant than areas affected by subgrain rotation, and they are characterized by grains with irregular shape, large-amplitude grain boundary sutures, and grain sizes between 100 and 500 µm (Fig. 6D). In grain boundary migration–controlled zones, some recrystallized grains appear nearly strain free, while other grains have patchy or sweeping undulose extinction. Pinning caused by mica is common in these zones (Fig. 6E), indicating recrystallization occurred at the lower-temperature range for grain boundary migration, since pinning is typically absent for high-temperature grain boundary migration (Stipp et al., 2002b). Other areas show a mixture of fabric elements, including equant grains and subgrains of uniform size mixed with irregular, amoeboid-shaped grains with a broad range in recrystallized grain sizes, suggesting contributions of both subgrain rotation and grain boundary migration. Together, these observations suggest recrystallization occurred at the transition between subgrain rotation and grain boundary migration, indicating deformation temperatures of ~500 °C (Stipp et al., 2002b) and corresponding to regime 3 of the experimental dislocation creep regimes of Hirth and Tullis (1992).

There are two generations of microfractures that crosscut these veins. Generation-one fractures are filled by either calcite or secondary phases and preceded dynamic recrystallization of the veins (Figs. 6F and 7D); these fractures stop at the edge of the quartz vein and are truncated by the matrix foliation. Generation-two fractures crosscut the recrystallization fabrics in quartz veins, aggregates of secondary phases, and the matrix foliation (Fig. 6F); these fractures are considered late-stage extensional fractures (tension gashes), as their opening direction consistently parallels the direction of instantaneous extension associated with foliation and boudinage structures.

Secondary mineral assemblage. Secondary phases consist of phengitic muscovite + chlorite + biotite + tourmaline + rutile ± microcline ± dolomite (Table 2). The secondary assemblage is considered to be in local chemical equilibrium (Thompson, 1959) because phases are consistently in contact with each other, they do not have reaction rims or replacement structures, and microprobe data demonstrate each phase has a consistent composition (Appendix 2; see footnote 1). The secondary assemblage occurs in varying concentrations in each South Summit sample. In sample EV6a, secondary phases occur on either side of the large deformed quartz vein as 1–2-mm-thick aggregates of muscovite, chlorite, rutile, and tourmaline (Fig. 7A); euhedral dolomite grains up to ~800 µm in diameter were observed filling a large fracture in the quartz vein as well. In EV6c, the assemblage is less abundant, but it exists as elongate domains of muscovite, and small tourmaline grains averaging ~20 µm in size, as well as one occurrence of microcline.

TABLE 2. AVERAGED ELECTRON MICROPROBE DATA FOR SECONDARY PHASES IN SOUTH SUMMIT SAMPLES

Major oxides (wt%)	Muscovite	Chlorite	Tourmaline	Biotite
SiO_2	45.68	25.55	37.52	36.41
TiO_2	0.50	0.49	0.51	1.61
Al_2O_3	33.01	22.27	34.17	18.01
FeO	2.59	21.07	6.31	16.97
MnO	0.01	0.01	0.00	0.02
MgO	2.21	15.87	7.46	11.91
CaO	0.01	0.03	0.99	0.19
Na_2O	0.30	0.12	2.10	0.11
K_2O	10.38	0.09	0.05	9.12
Cr_2O_3	0.05	0.02	0.04	0.06
Cl	0.01	0.01	0.02	0.04
BaO	0.39	0.01	0.02	0.09
F	0.00	0.27	0.00	0.87
H_2O (calculated)	4.44	11.24	3.81	3.54
B_2O_3 (calculated)	N/D	N/D	11.05	N/D
Total:	99.59	97.07	104.05	98.94

Note: N/D—not determined.

The secondary assemblage is best exhibited in sample EV6b, where phases occur within fractures in the large quartz vein (Fig. 7D), as individual grains within the matrix (Figs. 6B and 7B), or as elongate, foliation-parallel aggregates ranging between a few millimeters to a few centimeters in length (Fig. 7C). Muscovite is the most abundant secondary phase and may occur as scaly aggregates or exist as individual grains between 50 and 200 µm in length (Figs. 6B and 7C–7F). There are populations of undeformed and deformed muscovite, with undeformed grains appearing to have neocrystallized in the later stages of deformation (Figs. 6B and 7F). Chlorite commonly forms aggregates of flaky, gray-green grains between 20 and 200 µm in length that generally occur proximal to aggregates of muscovite (Fig. 7C) and, based on textural relationships, are considered a part of the secondary assemblage rather than forming as a late-stage replacement. Swarms of foliation-parallel biotite that average 150 µm in length are present in certain zones of the matrix, typically near aggregates of muscovite and chlorite (Fig. 7B). They occur as interstitial grains that may be bent or pinched-out by matrix calcite and quartz grains that grew statically. Tourmaline grains between 50 and 200 µm in length occur within the aggregates of muscovite and chlorite, and in the matrix proximal to other secondary phases (Figs. 7B, 7D, 7F, and 8A–8B). The long axis of tourmaline grains consistently lies within the foliation plane, but it is either parallel to the extension direction or normal to it. Rutile exists mostly within aggregates of secondary phases as well-defined acicular grains between 10 and 80 µm long and as blocky, anhedral grains up to 250 µm in diameter (Figs. 7D and 7F). Also present in aggregates of secondary phases are small (<15 µm), high-relief grains with optical properties and energy-dispersive spectra indicative of epidote or vesuvianite.

Origin and Equilibration of Secondary Phases

Tourmaline is a complex borosilicate mineral with 31 currently recognized species making up the tourmaline supergroup (Dutrow and Henry, 2014). These minerals are valuable petrogenetic indicators due to their systematic response to chemical changes in coexisting minerals and fluids, and pressure-temperature conditions (Henry and Dutrow, 1996; Dutrow and Henry, 2011; Hawthorne and Dirlam, 2011; van Hinsberg et al., 2011a, 2011b; Henry and Dutrow, 2012). Tourmaline grains in South Summit samples are euhedral, lack a detrital nucleus, and sometimes have mineral inclusions abundant in the interior of the grain (Figs. 8A–8B). Electron microprobe transects of tourmaline grains show some degree of

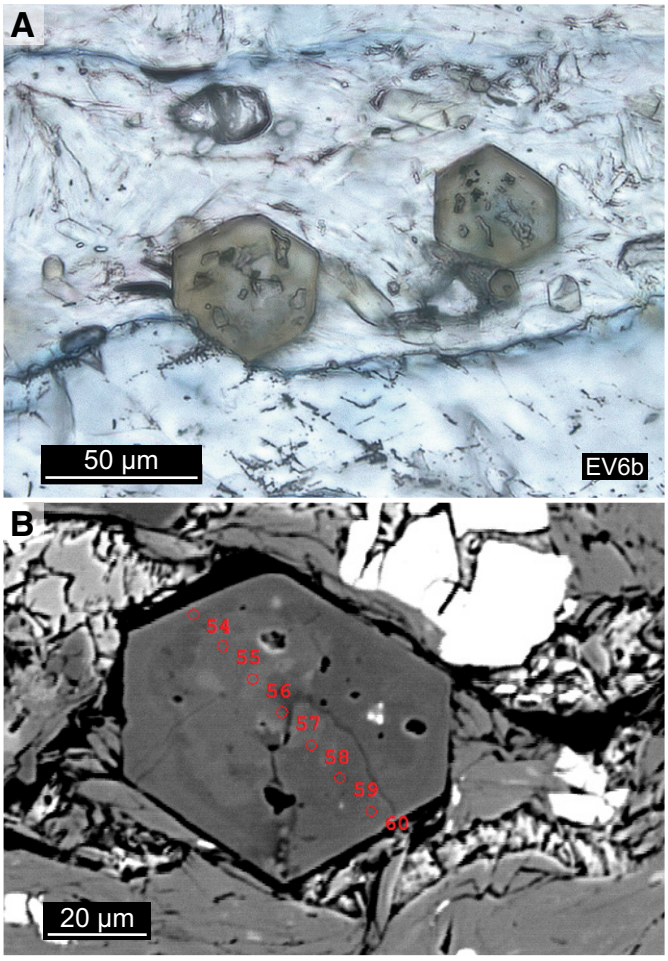

Figure 8. (A) Plane polarized light photomicrograph of euhedral secondary tourmaline grains found in South Summit samples. (B) Backscattered-electron image of a tourmaline with red dots specifying the location of electron microprobe spot analyses. Microprobe composition data indicate dravite is the species of tourmaline (see Fig. 9; Table 3).

TABLE 3. ELECTRON MICROPROBE TRANSECT ACROSS A TOURMALINE GRAIN IN PART OF THE SECONDARY ASSEMBLAGE IN SOUTH SUMMIT SAMPLE EV6B

Major oxides (wt%) Spot no.	54	55	56	57	58	59	60
SiO_2	31.71	37.09	38.02	36.69	38.14	39.25	38.21
TiO_2	0.65	0.42	0.30	0.49	0.35	0.09	0.71
Al_2O_3	25.60	35.61	35.44	32.48	34.23	33.98	34.77
FeO	4.61	7.22	8.26	7.82	5.61	5.32	6.01
MnO	0.01	0.02	0.00	0.00	0.00	0.00	0.00
MgO	6.13	6.94	6.01	7.56	8.53	8.36	7.71
CaO	5.19	0.44	0.10	2.09	1.21	0.88	0.57
Na_2O	1.64	2.22	2.22	1.47	1.83	2.15	2.27
K_2O	0.15	0.04	0.03	0.03	0.05	0.02	0.06
Cr_2O_3	0.01	0.02	0.00	0.02	0.05	0.01	0.02
Cl	0.14	0.02	0.02	0.07	0.01	0.00	0.00
BaO	0.00	0.00	0.00	0.00	0.00	0.04	0.01
F	0.00	0.00	0.00	0.00	0.00	0.00	0.00
H_2O (calculated)	3.15	3.83	3.85	3.73	3.86	3.88	3.88
B_2O_3 (calculated)	9.22	11.12	11.16	10.86	11.20	11.26	11.23
Total:	88.20	104.98	105.40	103.32	105.08	105.23	105.44
Tourmaline species:	Uvite	Dravite	Dravite	Dravite	Dravite	Dravite	Dravite

Note: Spot locations for the tourmaline grain analyzed are shown on the backscattered-electron image in Figure 8B.

compositional zoning (Fig. 8B; Table 3). The only major compositional disparity found was a spot analysis that had a more Ca-rich composition (spot number 54; Fig. 8B; Table 3), which is consistent with the Ca-rich bulk composition of the rock. The mineral inclusions found in many tourmalines are typical of rapid growth at low temperatures, while the euhedral rim likely represents growth and reequilibration at peak temperatures (Henry and Dutrow, 1996). All chemical composition data, normalized using the 15 Y+T+Z site-normalization scheme of Henry and Dutrow (1996), consistently indicate that dravite is the species of tourmaline present (Table 3; Fig. 9).

In the schorl-dravite solid solution series, dravite is the Mg-rich end member, and it is a species of tourmaline commonly found in metamorphosed limestones and dolostones with metasomatically introduced boron (B; Henry and Dutrow, 1996). It is possible and quite common, however, to have diagenetic tourmaline without a detrital nucleus in carbonate rocks (Srivastava and Schnitzer, 1976; van Hinsberg et al., 2011a), but such occurrences are generally the X-site–vacant foitite or magnesio-foitite species (Henry et al., 1994; Rosenberg and Foit, 2006). South Summit tourmalines are very similar in character and style of occurrence to those in metapelitic rocks described in a study by Dutrow et al. (1999), where extensive infiltration of fluids, sourced from a nearby granitic intrusion, caused anomalously high concentrations of chemically homogeneous tourmalines without detrital cores. Indeed, the highly concentrated and localized nature of dravite in South Summit samples, and the fact that grains are chemically homogeneous, suggests precipitation occurred all at once from a large influx of B-rich fluid (Dutrow et al., 1999; Henry and Dutrow, 1996).

The way in which fluids chemically reacted with the summit limestone is interpreted in terms of the secondary parageneses and the composition of the Qomolangma Formation protolith, based on summit and Hillary Step samples. As mentioned already, the invasive fluid would have been enriched in B; however, an unknown amount of B would have also been released upon dissolution of detrital white mica and clay (Lerman, 1966; Couch and Grim, 1968). The breakdown of mica and clays from the protolith would have also released some amount of K and Al, while Mg would have become available upon the dissolution of dolomite. CL images of summit and Hillary Step samples indicate elevated amounts of trace Ti in detrital quartz grains (Rusk et al., 2006). Since Ti is a relatively immobile element in most hydrothermal settings and titanous, detrital heavy minerals (e.g., rutile, anatase, brookite, etc.) were not directly observed in summit or Hillary Step samples, the Ti needed to stabilize rutile would have originated from the dissolution of titanous detrital quartz grains. Also, quartz veins are dissolved at points of contact with aggregates of secondary phases, demonstrating Si was derived from these veins as well as detrital grains. While these local sources would have been important, especially for immobile phases Al and Ti, the invasive fluids are thought to have introduced most of the B, Fe, K, and H_2O required to stabilize secondary phases.

Although rutile and tourmaline would have been engaged in equilibration reactions in the rock, the significant parageneses involved are considered to be phengitic muscovite, chlorite, and biotite, which are related in the KFMASH system by the biotite isograd reaction:

$$\mathrm{Chl} + \mathrm{Kfs} = \mathrm{Bt} + \mathrm{Ms}\ (+\mathrm{Qtz} + \mathrm{H_2O}).$$

Below the isograd, chlorite and K-feldspar are stable and, during progressive metamorphism of pelitic rocks, will react to produce phengitic

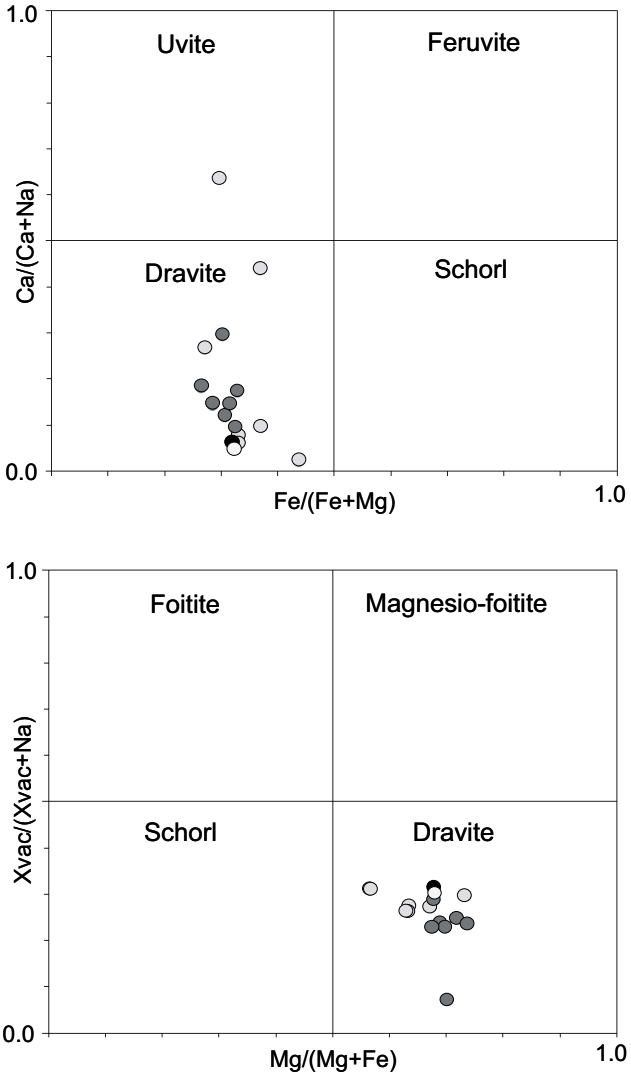

Figure 9. Microprobe data from four tourmaline grains plotted on compositional variation diagrams. The varying gray shades correlate to the different grains analyzed, two of which were microprobe transects.

muscovite and biotite in the presence of excess quartz and water (Spear, 1993; Bucher and Grapes, 2011). Because there is essentially no K-feldspar present in South Summit samples, biotite would have formed in a continuous reaction with muscovite and chlorite (Fig. 10; Spear, 1993). In pelitic compositions, at pressures between 3.5 and 4.5 kbar, this occurs above 440 °C, with chlorite reacting out of the rock to form kyanite and biotite between 550 °C and 600 °C, depending on the Mg content of the rock. At lower pressures (<3 kbar), biotite will form at slightly lower temperature (~400 °C), and cordierite will appear with this assemblage between 500 °C and 550°C (Bucher and Grapes, 2011). The Si-content in phengitic muscovite has been shown to correlate positively with pressure (Velde, 1967; Massonne and Schreyer, 1987; Zhu and Wei, 2007). The averaged Si content for muscovite in South Summit samples is 3.09 per formula unit, which would correlate to ~3 kbar, assuming an average metapelitic composition for the secondary assemblage.

Flow Stress Calculations

Calcite was not used for flow stress calculations due to evidence of late-stage static growth. Instead, portions of the quartz vein in EV6b that recrystallized by subgrain rotation were analyzed to estimate flow stress using the quartz recrystallized grain-size piezometer of Stipp and Tullis (2003), modified after Holyoke and Kronenberg (2010), for climb-accommodated dislocation creep. Grain-size data yield average recrystallized grain sizes between 25 and 35 μm, which correspond to paleodifferential stresses of 29–38 MPa. Using the same piezometer, Law et al. (2011) calculated similar values for samples collected from the footwall of the South Tibetan detachment in the Rongbuk Valley. Their results showed differential stresses of 10–15 MPa for rocks 100–550 m beneath the detachment, increasing to 25–35 MPa for rocks <50 m beneath the detachment. A major caveat of this comparison lies in the assumption that the recrystallization fabrics analyzed in both studies are related to the same phase of deformation and faulting under similar temperatures, strain rate, and water content.

Ti-in-Biotite Geothermometry

The amount of trace Ti in metamorphic biotite has been shown to increase as a function of temperature (Henry and Guidotti, 2002), which is the basis for the Ti-in-biotite geothermometer. For the best results, the paragenesis must be similar to that of calibration samples used by Henry and Guidotti (2002) and Henry et al. (2005), and should have been equilibrated between ~3 and 6 kbar. Secondary minerals of proper chemical

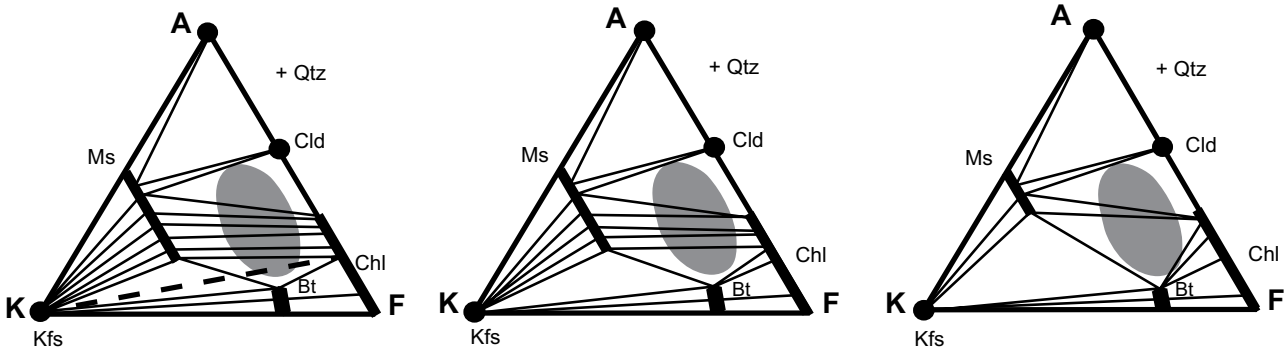

Figure 10. Using the formulation of Spear (1993), this series of AKF diagrams (e.g. Winter, 2001) illustrates the migration of the muscovite-biotite-chlorite (Ms-Bt-Chl) and K-feldspar–biotite (Kfs-Bt) subtriangles to more aluminum (Al)–rich compositions by continuous reactions in the biotite zone, above the biotite isograd. Figure is after Winter (2001, their Fig. 28-4). Cld—Chloritoid; Qtz—quartz.

character include quartz, chlorite, rutile, and muscovite, all of which are present in South Summit samples and appear to be in local chemical equilibrium with biotite.

The composition data, from what were considered the best microprobe analyses of biotite in EV6b (Appendix 2; see footnote 1), were averaged and used for geothermometry calculations. Following the methods of Henry et al. (2005), using a 24 anion normalization, the calculated temperature is 603 °C ± 25 °C. The accuracy of the Ti-in-biotite thermometer, in this study, in part hinges on the pressure at which biotite and other secondary phases equilibrated. An averaged muscovite Si -content of ~3.1 per formula unit suggests that pressures during equilibration were ~3 kbar, which is sufficient for this thermometer. If equilibration occurred at <3 kbar, the calculated temperature may be inflated due to the increase in solubility of Ti in biotite with decreasing pressure. Still, using the Ti-in-biotite geothermometer conservatively, temperatures at the time secondary phases equilibrated are thought to have reached ~500 °C.

Ti-in-Quartz Geothermometry (TitaniQ)

Similar to biotite, the amount of trace Ti in quartz increases with temperature of crystallization or recrystallization (Wark and Watson, 2006). Initial application of the TitaniQ geothermometer was thought to be restricted to quartz crystallized at ≥400 °C, or recrystallized through high-temperature grain boundary migration. However, recent studies have shown that this thermometer is useful down to temperatures of ~350 °C and that recrystallization through grain boundary bulging is also capable of equilibrating Ti concentrations in quartz (Haertel et al., 2013). Electron microprobe data gathered from the deformed quartz veins found in samples EV6a and EV6b (Table 4) were used for TitaniQ geothermometry following the methods of Wark and Watson (2006) and Thomas et al. (2010). Measuring low concentrations of Ti, below ~10–15 ppm, is problematic with an electron microprobe, and spot analyses yielding concentrations below detection limits were not used for TitaniQ calculations.

All calculations were done using the refined formula of Thomas et al. (2010), which is:

$$RT \ln X\mathrm{TiO}_2 = -60{,}952 + 1.520 \times T - 1741 \times P + RT \ln a\mathrm{TiO}_2, \quad (1)$$

where R is the gas constant 8.3145 J/K, T is temperature in Kelvin, P is pressure and is inferred to be 3 kbar, $X\mathrm{TiO}_2$ is the mole fraction of TiO_2 in quartz, and $a\mathrm{TiO}_2$ is the activity of TiO_2 in the system. Since rutile is abundantly present in both samples, calculations were done using a TiO_2 activity of 1, following the general assumption of Wark and Watson (2006) and Thomas et al. (2010) that if rutile is present, activity is effectively 1.

Due to sample charging, data from sample EV6a are limited to three spot analyses acquired from the center part of the vein, in an area characterized by large prismatic subgrains (Fig. 11A). All three spot locations yielded Ti concentrations well above detection limits, and the averaged concentration yields a temperature of 624.6 °C (Table 4). In sample EV6b, data were collected from four locations, two of which (D and F) were composed of detrital quartz grains and quartz fragments not a part of the large deformed vein; data from these locations were therefore omitted. Location E was composed of four spot analyses, all of which were below the Ti detection limit (Table 4). Six spot analyses were acquired from location G, two of which were below the Ti detection limit. The averaged concentrations from the remaining four analyses at location G yields a temperature of 511.9 °C (Table 4). Importantly, location G occurs adjacent to secondary phases, dominantly white mica and tourmaline in high concentration in the matrix, and displayed recrystallization fabrics characterized by grain boundary sutures and subgrain development (Fig. 11B).

TABLE 4. ELECTRON MICROPROBE DATA FROM QUARTZ VEINS IN SOUTH SUMMIT SAMPLES USED FOR TITANIQ GEOTHERMOMETRY

Sample	Spot ID	Ti concentration (wt%)	Ti (ppm)	Detection limit (ppm)	
EV6a	B-1	0.0219	219	15	
EV6a	B-2	0.0100	100	15	
EV6a	B-3	0.0086	86	15	
		Averaged Ti:	135 ppm	Temp:	624.6 °C*
EV6b	D-1	0.0227	227	14	
EV6b	D-2	0.0159	159	13	
EV6b	D-3	0.0013	13	16	
EV6b	D-4	0.0017	17	15	
EV6b	D-5	0.0018	18	16	
EV6b	D-6	0.0021	21	16	
EV6b	D-7	0.0009	9	15	
EV6b	D-8	0.0007	7	15	
EV6b	D-9	0.0342	342	16	
EV6b	D-10	0.0239	239	15	
EV6b	D-11	0.0284	284	16	
EV6b	D-12	0.0095	95	15	
EV6b	E-1	0.0012	12	15	
EV6b	E-2	0.0005	5	15	
EV6b	E-3	0.0009	9	15	
EV6b	E-5	0.0009	9	15	
EV6b	F-1	0.0010	10	15	
EV6b	F-2	0.0006	6	15	
EV6b	F-3	0.0004	4	15	
EV6b	F-4	0.0003	3	16	
EV6b	F-5	0.0005	5	15	
EV6b	F-6	0.0014	14	15	
EV6b	F-7	0.0017	17	15	
EV6b	F-8	0.0010	10	15	
EV6b	F-10	0.0008	8	15	
EV6b	G-1	0.0078	78	15	
EV6b	G-2	0.0033	33	16	
EV6b	G-3	0.0016	16	15	
EV6b	G-5	0.0009	9	16	
EV6b	G-6	0.0005	5	16	
EV6b	G-7	0.0024	24	16	
		Averaged Ti:	37.8 ppm	Temp:	511.9°C*

Note: Rows shaded in gray were used for TitaniQ calculations; all others were omitted for reasons discussed in the text.
*Temperature calculated at 3 kbar.

$^{40}Ar/^{39}Ar$ GEOCHRONOLOGY

Sample Characterization

Grains of phengitic muscovite used for $^{40}Ar/^{39}Ar$ dating by incremental heating were extracted from aggregates of secondary phases found on the outside of sample EV6a (Fig. 7A). The aggregates contain muscovite, chlorite, tourmaline, and rutile, with muscovite being the volumetrically dominant phase (Figs. 7E–7F). Optically, secondary phases in EV6a have identical characteristics to those in other South Summit samples, and we interpret their origin and timing of crystallization to be the same in each sample. In cross section, the aggregates range from a few millimeters up to 4 cm in length and fluctuate in thickness between 0.5 and 2 mm. The alignment of muscovite defines a foliation that parallels the vein margins and contours around asperities of the vein edge.

Based on differences in texture and grain size, muscovite can be divided into two populations. Population-one contains grains between 100 and 200 μm in length that are weakly to significantly deformed (Fig. 7E). Deformed grains have sweeping extinction, are bent or kinked, and in

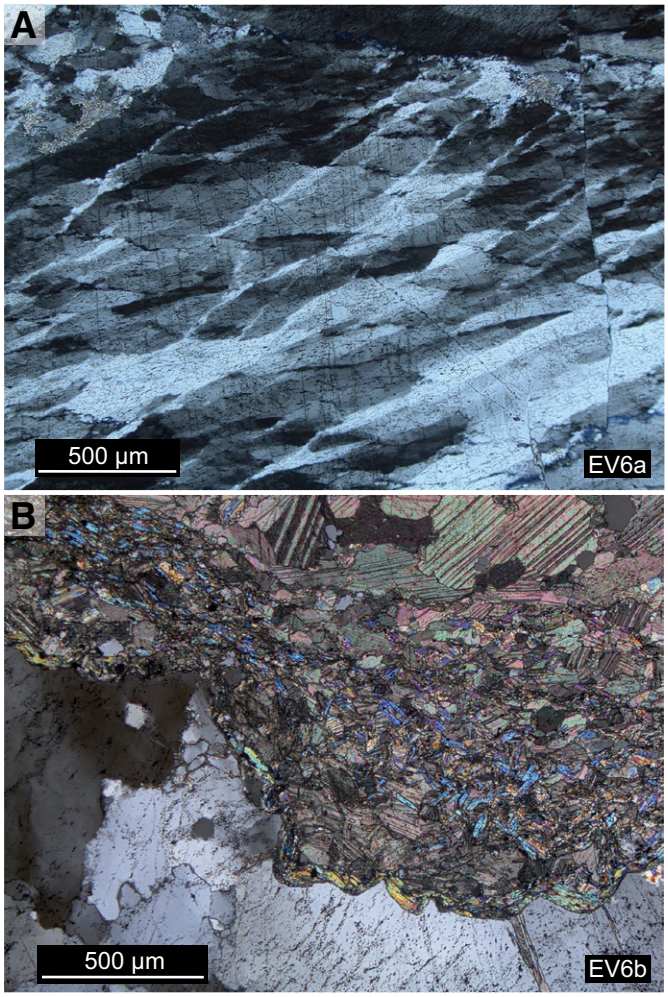

Figure 11. Photomicrographs showing where electron microprobe data used for TitaniQ geothermometry were gathered from the quartz veins in samples EV6a and EV6b. (A) Data was acquired from the central portion of the image and yielded an average temperature of 624.6 °C (Table 4). (B) Data acquired from this portion of the vein (location G) yielded an average temperature of 511.9 °C (Table 4). There is a significant amount of muscovite and tourmaline in the matrix adjacent to the vein; small amounts of biotite and chlorite were observed as well.

some places have been partly recrystallized. Population two is more fine-grained and is composed of neocrystallized grains 30–100 µm in length, which are aligned with the dominant foliation and are relatively undeformed (Figs. 6B and 7F). The nature of occurrence and undeformed character of neocrystallized grains suggest they formed in the final phases of deformation and fabric development, whereas population one would have formed pre- to syndeformation.

Results and Interpretation

Results from incremental heating show a monotonically rising age spectrum with apparent ages between 18 and 28 Ma for 95% of ^{39}Ar released (Fig. 12; Appendix 3; see footnote 1). A younger apparent age of 15 Ma was obtained during the first 1% of ^{39}Ar released, while apparent ages above 28 Ma (31–30 Ma) were obtained for the final 4% of degassing. Results do not indicate the release of argon from minerals other than white mica, and electron microprobe analysis shows that white mica compositions are consistently phengitic (Table 2; Appendix 2; see footnote 1). Since the Qomolangma Formation was deposited in the Ordovician (e.g., Myrow et al., 2009), the possibility of contamination from detrital mica is precluded by ^{40}Ar/^{39}Ar results of Cenozoic age. The age spectrum is not thought to be affected by excess argon either, since incorporation of excess argon is not common in white mica, except when formed at high pressure (Li et al., 1994; Arnaud and Kelley, 1995), and given the absence of a "saddle" in the age spectrum (McDougall and Harrison, 1999)

The lack of an obvious age plateau and the staircase shape of the ^{40}Ar/^{39}Ar age spectrum are typical for synkinematic micas dated from mylonites (e.g., Kirschner et al., 1996). It has been shown that such spectra may be the result of neocrystallization or recrystallization of muscovite during ductile deformation and mylonitization (Dunlap et al., 1991; Cosca et al., 1992; Kirschner et al., 1996; Dunlap, 1997), or diffusional argon loss in populations of variably deformed grains (Mulch et al., 2002; Mulch and Cosca, 2004). Some suggest that the range of ages dates the interval of neocrystallization and growth of mica (Kirschner et al., 1996), and when ductile deformation ceased (Dunlap, 1997). For argon loss by diffusion, there is no single closure temperature that is appropriate for a population of deformed grains because heterogeneity in deformation microstructures guarantees that diffusion length scales, and thus diffusivity, will vary across the grain population (Mulch et al., 2002; Mulch and Cosca, 2004). The effect this can have on age spectra is particularly compounded when cooling is protracted through the argon closure "window" (Dunlap, 1997), because deformation microstructures will serve as intragrain fast diffusion pathways (Mulch et al., 2002). This results in populations of muscovite with differing argon concentration gradients that consequently generate a range of apparent ages during incremental heating, which can lead to a staircase-shaped age spectrum.

Therefore, the 10 m.y. range in apparent ages is interpreted to reflect the different coexisting populations of muscovite and their different times of development. The oldest apparent age of ca. 28 Ma is associated with gas released at the highest-temperature steps from the cores of the least-deformed grains in population one and estimates the timing of crystallization of muscovite and other secondary phases. This interpretation implies that there were no subsequent thermal events above the closure temperature for argon diffusion in muscovite (~400 °C; Harrison et al., 2009). The youngest apparent age of ca. 18 Ma is associated with gas released during the lowest-temperature steps from the smallest neocrystallized grains in population two. Because neocrystallized grains formed in the final phases of deformation, as suggested by their undeformed fabric-parallel nature, ca. 18 Ma is considered to date the end of ductile deformation at the South Summit. Gébelin et al. (2013) reported that low hydrogen isotope ratios (δD) for biotite and hornblende, in mylonitic samples collected from the detachment footwall in Rongbuk Valley, indicate that meteoric fluids penetrated the South Tibetan detachment during mylonitization in the late early Miocene. This is important because such fluids would have promoted rehydration reactions and neocrystallization of muscovite, even at low deformation temperatures. The remaining intermediate apparent ages likely reflect gas released from a combination of recrystallized grains, earlier neocrystallized grains, and grains that lost argon by diffusion, notably in the deformed grains.

PETROGENESIS

Upper Qomolangma Formation—Summit Samples

Shortly after India's collision with Asia between 54 and 50 Ma (Green et al., 2008), deformation was accommodated by folding and thrusting

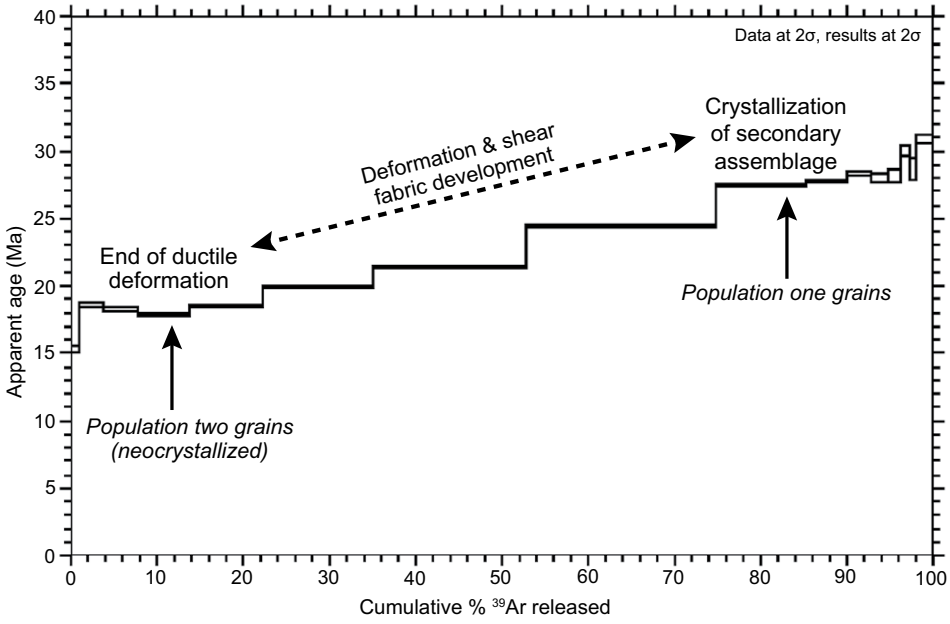

Figure 12. $^{40}Ar/^{39}Ar$ age spectrum for muscovite. Grains were extracted from large aggregates of secondary phases along the edge of the deformed quartz vein in EV6a (Fig. 7A). The specimen was composed of different populations of muscovite grains, including deformed, recrystallized and neocrystallized grains, which resulted in the staircase nature of the age spectrum.

within the Tethyan Sedimentary Sequence (Fig. 13A), resulting in significant upper-crustal thickening in the central Himalaya by the middle Eocene to early Oligocene (Colchen et al., 1986; Godin et al., 1999a, 1999b, 2001; Godin, 2003; Murphy and Yin, 2003; Aikman et al., 2008; Kellett and Godin, 2009). In many locations, evidence of this is preserved in the base of the Tethyan Sedimentary Sequence by top-to-the-south structures that are generally interpreted as evidence for south-directed thrusting prior to the onset of north-directed detachment faulting (e.g., Vannay and Hodges, 1996; Coleman and Hodges, 1998; Godin et al., 2001).

Microstructure and fabric-based results show that temperatures reached at least 250 °C during deformation and mylonitization of summit samples. As previously discussed, fission-track data of Streule et al. (2012), from a summit sample, suggest that the Qomolangma Formation was exhumed through the apatite fission-track closure temperature (130 °C ± 30 °C) by 30.5 ± 5.1 Ma, implying that summit samples were deformed prior to this date. Therefore, the well-developed mylonitic foliation and low-grade metamorphism (≥250 °C) preserved in summit samples are the result of Eohimalayan thrusting, folding, and crustal thickening of the Tethyan Sedimentary Sequence (Fig. 13A). This interpretation is consistent with other studies that suggest rocks in the hanging wall of the South Tibetan detachment reached 300–400 °C during regional metamorphism associated with upper-crustal shortening (e.g., Schneider and Masch, 1993; Garzanti et al., 1994; Guillot et al., 1995; Cottle et al., 2011).

The only evidence of younger deformation in summit samples is seen as crosscutting fractures and as unimodal aggregates of secondary dolomite that overprint fabric. Unimodal grain size of replacement dolomite is suggested by Sibley and Gregg (1987) to indicate a single dolomite nucleation event on a unimodal carbonate substrate. Scoffin (1987) proposed that secondary dolomitization that is fabric destructive forms at higher fluid flow rates, compared to fabric-preserving dolomitization. This would imply that dolomite replacement happened during one event from a fluid that infiltrated the Qomolangma Formation at a relatively high rate. These hydrothermal fluids may have been related to the metasomatic event recorded in South Summit samples, whereas fractures, which crosscut fabric, and the aggregates of dolomite are likely the result of exhumation and detachment faulting.

Lower Qomolangma Formation—South Summit Samples

The range of apparent $^{40}Ar/^{39}Ar$ ages lies within the time span of Neohimalayan metamorphism, crustal anatexis, and movement on the South Tibetan detachment. As previously discussed, the apparent $^{40}Ar/^{39}Ar$ age of ca. 28 Ma (Fig. 12) is interpreted to estimate the timing of crystallization of the secondary assemblage, associated with metasomatism. Since secondary phases equilibrated at temperatures of ~500 °C, and the Qomolangma Formation was presumably already exhumed and cooled below ~130 °C by ca. 30.5 Ma (Streule et al., 2012), these "peak" temperatures would have been followed by rapid cooling in order to not reset the apatite fission tracks in the sample dated by Streule et al. (2012). The quenched nature and lack of retrograde textures in secondary phases corroborate that metasomatism was likely a brief, transient event caused by a pulse of hydrothermal fluid.

The abundance of dravite in South Summit samples suggests that metasomatism was caused by a B-rich fluid that infiltrated the base of the Qomolangma Formation. Such metasomatic fluids are typically derived as late-stage hydrothermal fluids exsolved from well-fractionated granitic melts that are unable to conserve B as tourmaline due to the limited quantity of AFM (AFM = Al-Fe-Mg) silicates available during the late stages of fractionation (Morgan and London, 1987; London et al., 1996, London, 1999). At the South Summit, for metasomatic fluids to have originated from granitic bodies requires that significant crustal melts were present by ca. 28 Ma. Leucosomes dated from the Everest region suggest Neohimalayan metamorphism had begun by 30–28 Ma (Viskupic and Hodges, 2001; Viskupic et al., 2005; Cottle et al., 2009), with concomitant anatectic melts forming in the Greater Himalayan Sequence by at least ca. 26 Ma (Viskupic et al., 2005; Jessup et al., 2008). Although these data indicate that Neohimalayan metamorphism was under way by ca. 28 Ma, they do not prove that significant melt had formed by that time.

Based on the available data, the metasomatic pulse recorded in South Summit samples is inferred to be associated with high-temperature, low-pressure Neohimalayan metamorphism between 30 and 28 Ma (Fig. 13B). This is envisaged to have occurred through the following sequence of events. During vapor-absent dehydration melting of muscovite and biotite

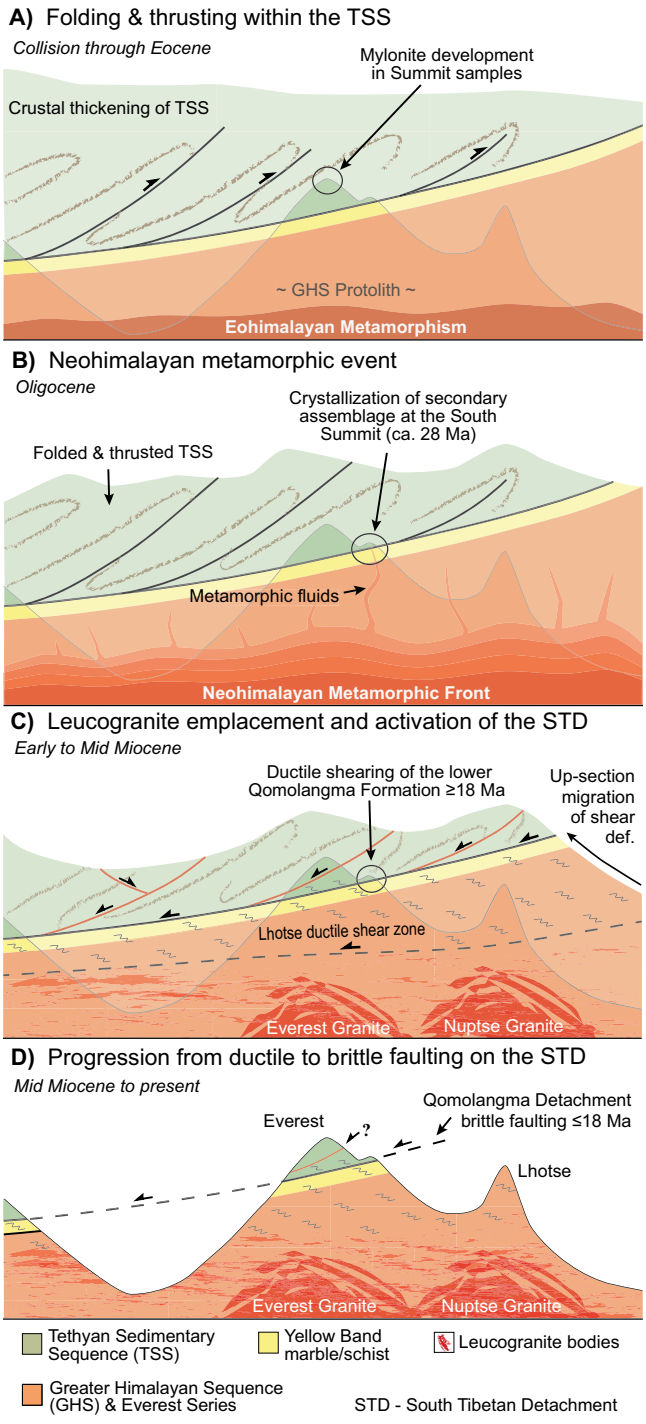

Figure 13. Tectonic evolution of the Qomolangma Formation and Qomolangma detachment. (A) Following India's collision with Asia, folding and thrusting of the Tethyan Sedimentary Sequence produced the well-developed mylonitic foliation in summit samples. (B) During peak Neohimalayan metamorphism, metamorphic fluids reached the lower Qomolangma Formation, leading to metasomatism and the crystallization of secondary phases in South Summit samples by ca. 28 Ma. (C) Up-section migration of the South Tibetan detachment and concomitant ductile shearing of the lower Qomolangma Formation, before ca. 18 Ma, produced the extensional shear fabrics seen in South Summit samples. (D) At the base of the Qomolangma Formation, ductile fabric development ceased by ca. 18 Ma and was followed by brittle faulting at the Qomolangma Formation–Yellow Band contact.

within the pelitic Greater Himalayan Sequence (Scaillet et al., 1990, 1996; Prince et al., 2001; Searle, 2013), B would have been liberated into aqueous solution upon decomposition of micas (Grew, 1996; Henry and Dutrow, 1996), particularly by muscovite dehydration reactions. As peak metamorphic conditions were reached, the liberation and sequestration of B from micas into newly formed tourmaline grains would have been nearly complete within the Greater Himalayan Sequence (Henry and Dutrow, 1996; van Hinsberg et al., 2011a). However, while B released from micas would have largely been preserved within the Greater Himalayan Sequence as tourmaline, the highly mobile nature of B and the partitioning of B into fluids generated by dehydration of micas could have led to the migration of B and other volatiles away from the source region. This is especially true for peak metamorphic conditions, since the minimum B content in fluid required to stabilize tourmaline increases significantly with temperature (Weisbrod et al., 1986). In most circumstances, when such fluids pervade the surrounding wall rock, significant tourmaline formation may proceed, which is the most common cause of tourmaline growth on the retrograde path (van Hinsberg et al., 2011a). The transport of mobile metamorphic fluids over great distances will occur when devolatilization reactions generate fluid pressures large enough to hydraulically fracture the surrounding rock, creating pathways for fluid migration (Walther and Orville, 1982; Yardley, 1997). During Neohimalayan metamorphism, muscovite dehydration within the Greater Himalayan Sequence would have led to significant fluid pressure gradients. Given that fracture propagation relieves pressure, growth of fracture networks was probably episodic during discrete intervals of metamorphism. With progressive heating, continued devolatilization reactions, expansion of pore fluids, and episodic fracture propagation, upward metamorphic fluid flow proceeded along fracture networks and microcracks (Walther and Orville, 1980, 1982; Walther, 1990). Eventually, aqueous fluids enriched in B and other volatiles infiltrated the Tethyan Sedimentary Sequence, where metasomatic reactions proceeded. At the base of the Qomolangma Formation, the result of metamorphism and devolatilization within the Greater Himalayan Sequence is manifested by significant tourmaline formation and retrograde rehydration reactions, reflected in the secondary assemblage (Fig. 13B).

If, at some point following metasomatism, a structurally higher detachment cut across the summit limestone above the South Summit, as depicted in Figures 13C and 13D, it would have augmented the steep geothermal gradient between upper Qomolangma Formation rocks and the metasomatically altered rocks of the lower Qomolangma Formation. The shear fabrics and elongate quartz and calcite grains in Hillary Step samples suggest that some amount of shear displacement was accommodated within the middle Qomolangma Formation.

Upper and Lower Qomolangma Formation Comparison

There are three important differences between summit and South Summit samples that indicate their fabrics are not related to the same phase of deformation. (1) There is almost no evidence of extensional deformation in summit samples, whereas South Summit samples show many examples of boudinage (Figs. 6A and 7F) and extensional "generation-two" fractures (Fig. 6F). (2) Summit samples yield a high flow stress estimate of ~126 MPa, which is nearly four times higher than estimates obtained from samples collected proximal to the Qomolangma detachment, i.e., 29–38 MPa at the South Summit (this study) and 25–35 MPa in the Rongbuk Valley (Law et al., 2011). (3) Temporal constraints on deformation provided by apatite fission-track data from the upper Qomolangma Formation suggest deformation of summit samples occurred at >30.5 Ma (Streule et al., 2012), while $^{40}Ar/^{39}Ar$ data from the lower Qomolangma Formation indicate deformation of South Summit samples occurred between 28 and 18 Ma.

IMPLICATIONS FOR THE QOMOLANGMA DETACHMENT

Pervasive shear fabrics in South Summit samples show that the Qomolangma detachment was initially active as a distributed shear zone within the lower portion of the Qomolangma Formation on Mount Everest. A progression from ductile to brittle faulting is microstructurally demonstrated by extensional, generation-two fractures in South Summit samples (Fig. 6F), which show that the orientation of instantaneous extension associated with ductile fabrics did not change as deformation progressed into the brittle regime.

Sakai et al. (2005) described an exposure of the Qomolangma detachment on the northeast ridge of Everest as a damage zone extending 5 m above and below the fault plane, with a 5–40-cm-thick breccia zone at the base of the Qomolangma Formation. However, in South Summit samples, the only evidence for brittle activity on the Qomolangma detachment is crosscutting fractures and tension gashes (Fig. 6F). The fact that South Summit samples were collected ~15 m above the detachment, outside of the damage zone observed by Sakai et al. (2005), may explain the lack of a cataclastic overprint in these samples.

The $^{40}Ar/^{39}Ar$ spectrum, coupled with petrographic observations of the different populations of white mica, suggests that ductile shearing at the base of the Qomolangma Formation was ongoing until ca. 18 Ma (e.g., Kirschner et al., 1996; Dunlap, 1997). At this time, temperatures at the South Summit dropped below the plastic-brittle transition for calcite and below temperatures needed for thermally activated diffusive argon loss in muscovite (250–300 °C; Fig. 13D). However, in the Rongbuk Valley, Cottle et al. (2015) showed that ductile fabric formation associated with detachment faulting was ongoing until 16.4 Ma, and that brittle faulting is younger than 15.4 Ma. Given that the samples used in the present study were collected ~18 km updip from Rongbuk Valley, we advocate that the disparity in ages is merely due to the different structural positions represented in each study. Our study represents a shallower structural section using samples from the hanging wall of the Qomolangma detachment, whereas those used by Cottle et al., (2015) were collected from the footwall, 350 m below the detachment in Rongbuk Valley (Fig. 1). Past studies from the Everest region show that the age of shearing and mylonitization varies along the South Tibetan detachment, e.g., the well-exposed Dzakaa Chu section versus the Rongbuk section (see Murphy and Harrison, 1999; Cottle et al., 2007, 2011, 2015), with ages generally younging downdip to the north. Therefore, the $^{40}Ar/^{39}Ar$ data presented here are not intended to challenge the well-constrained ages of other studies and should merely be considered as a timing constraint for movement along the Qomolangma detachment specifically on the summit pyramid of Mount Everest.

Because of the consistent synkinematic nature of secondary phases and their association with metasomatic activity, we speculate that movement on the Qomolangma detachment was promoted by hydrothermal activity. It is well established that for slip to occur on low-angle detachments, there must be a mechanism that decreases the shear stress necessary to initiate faulting, i.e., reduces the effective stress (Hubbert and Rubey, 1959). Accordingly, hydrothermal fluids could have facilitated movement on the Qomolangma detachment by (1) increasing fluid pressure, thus reducing effective normal stress on the fault plane, and (2) hydrolytically and thermally weakening rocks proximal to the fault zone, thus reducing effective viscosity and promoting ductile failure. This scenario remains hypothetical, however, as results from this study cannot determine if influxes of hydrothermal fluids were reoccurring. In any case, given the gentle dip of the South Tibetan detachment and its proximity to footwall leucogranites throughout the orogen, we suggest that metamorphic or magmatic hydrothermal fluids facilitated activity of this structure.

CONCLUSIONS

Samples from the upper Qomolangma Formation have a well-developed mylonitic foliation and have undergone deformation at temperatures of ≥250 °C and flow stresses of ~126 MPa; at this structural level, the Qomolangma Formation is a calc-mylonite. At the base of the formation, samples record extensional shear deformation and a metasomatic event at temperatures of ~500 °C, which is envisaged to have occurred when dehydration reactions within the Greater Himalayan Sequence created fluid pressure gradients that drove volatile fluids upward into the overlying Tethyan Sedimentary Sequence. The increased temperatures at the South Summit and faulting on the Qomolangma detachment resulted in static growth of calcite and quartz, and mylonite development at flow stresses of ~34 MPa; here, the Qomolangma Formation is a marble mylonite and calc-schist.

Results from this investigation further refine the significance of the Qomolangma detachment on Mount Everest. The mylonitic foliation and extension-related microstructures in South Summit samples indicate that the Qomolangma detachment was not strictly a discrete brittle fault on Everest, but was initially active as a distributed shear zone within the lower portion of the Qomolangma Formation, at ≥18 Ma. Fabric-normal tension gashes in South Summit samples provide further evidence of a progression from plastic to brittle deformation, during which, the principal axis of instantaneous extension did not change.

The different fabrics and metamorphic temperatures observed between the upper and lower parts of the Qomolangma Formation are the result of distinct events that influenced the summit limestone at different times throughout Himalayan orogenesis. Fabrics seen in summit samples are the result of Eohimalayan deformation and low-grade metamorphism associated with initial thrust faulting, folding, and crustal thickening of the Tethyan Sedimentary Sequence in the Eocene. In contrast, the fabrics and elevated temperatures preserved in South Summit samples are the result of events that occurred in the late Oligocene and early Miocene, including metasomatism associated with Neohimalayan metamorphism and normal faulting on the South Tibetan detachment. This means that several significant tectonic events in Himalayan orogenesis are preserved in the Qomolangma Formation, a succession of deformed Ordovician limestone that now comprises the top of Mount Everest.

ACKNOWLEDGMENTS

Field and laboratory work was sponsored by an Expeditions Council Grant from National Geographic Society, the College of Letters and Science and Office of Research and Economic Development at Montana State University, and by graduate student research grants from the Geological Society of America and the Mazamas Foundation. We would like to thank the Earth Science Department at the University of Minnesota and Micah Jessup and graduate student Cameron Hughes at the University of Tennessee for their assistance with microprobe analyses; Darrell Henry at Louisiana State University for assistance with the Ti-in-biotite geothermometer, geochemical analysis of tourmaline, and for his manuscript review; Michael Cosca for $^{40}Ar/^{39}Ar$ dating and for reviewing an earlier version of the manuscript; and Mike Searle for his manuscript review. Sample collection would not have been possible without the efforts of Sherpa climbers Danuru Sherpa of Phortse and Jangbu Sherpa of Makalu, Nepal. Special thanks go to our expedition leader Conrad Anker for conceiving and organizing the expedition, and to Mr. Jiban Ghimire of Shangri-La Trekking. A major K–12 education/outreach program associated with the expedition was supported by National Science Foundation Experimental Program to Stimulate Competitive Research funding to the Extended University at Montana State, and Montana State University's Alumni Foundation. Thanks go to equipment sponsors, notably, The North Face, Black Diamond, and Trimble.

REFERENCES CITED

Aikman, A.B., Harrison, T.M., and Lin, D., 2008, Evidence for early (44 Ma) Himalayan crustal thickening, Tethyan Himalaya, southeastern Tibet: Earth and Planetary Science Letters, v. 274, p. 14–23, doi:10.1016/j.epsl.2008.06.038.

Armstrong, J.T., 1988, Quantitative analysis of silicates and oxide minerals: Comparison of Monte-Carlo, ZAF and phi-rho-Z procedures: San Fransisco Press, Microbeam Analysis, p. 239–246.

Arnaud, N.O., and Kelley, S.P., 1995, Evidence for widespread excess argon during high-pressure metamorphism in the Dora Maira (western Alps, Italy), using an ultra-violet laser ablation microprobe $^{40}Ar/^{39}Ar$ technique: Contributions to Mineralogy and Petrology, v. 121, p. 1–11, doi:10.1007/s004100050086.

Borghi, S., Castelli, D., Lombardo, B., and Visonà, D., 2003, Thermal and baric evolution of garnet granulites from the Kharta region of S Tibet, E Himalaya: European Journal of Mineralogy, v. 15, p. 401–418, doi:10.1127/0935-1221/2003/0015-0401.

Bucher, K., and Grapes, R., 2011, Petrogenesis of Metamorphic Rocks: Berlin, Springer-Verlag, 428 p., doi:10.1007/978-3-540-74169-5.

Burchfiel, B.C., Zhiliang, C., Hodges, K.V., Yuping, L., Royden, L., Changrong, D., and Jiene, X., 1992, The South Tibetan Detachment System, Himalayan Orogen: Extension Contemporaneous With and Parallel To Shortening in a Collisional Mountain Belt: Geological Society of America Special Paper 269, 41 p., doi:10.1130/SPE269.

Burg, J.P., and Chen, G.M., 1984, Tectonics and structural zonation of southern Tibet, China: Nature, v. 311, p. 219–223, doi:1038/311219a0.

Burkhard, M., 1993, Calcite twins, their geometry, appearance and significance as stress-strain markers and indicators of tectonic regime, a review: Journal of Structural Geology, v. 15, p. 351–368, doi:10.1016/0191-8141(93)90132-T.

Caby, R., Pêcher, A., and Le Fort, P., 1983, Le grande chevauchement central himalayen: Nouvelles données sur le métamorphisme inverse à la base de la Dalle du Tibet: Revue de Géographie Physiqueau et Géologie Dynamique, v. 24, p. 89–100.

Carosi, R., Lambardo, B., Molli, G., Musumeci, G., and Pertusati, P.C., 1998, The South Tibetan detachment system in the Rongbuk valley, Everest region. Deformation features and geological implication: Journal of Asian Earth Sciences, v. 16, p. 299–311, doi:10.1016/S0743-9547(98)00014-2.

Carosi, R., Lombardo, B., Musumeci, G., and Pertusati, P.C., 1999, Geology of the Higher Himalayan Crystallines in Khumbu Himal (eastern Nepal): Journal of Asian Earth Sciences, v. 17, p. 785–803, doi:10.1016/S1367-9120(99)00014-0.

Catlos, E.J., Harrison, T.M., Manning, C.E., et al., 2002, Records of the evolution of the Himalayan orogen from in situ Th-Pb ion microprobe dating of monazite: Eastern Nepal and western Garhwal: Journal of Asian Earth Sciences, v. 20, p. 459–479, doi:10.1016/S1367-9120(01)00039-6.

Colchen, M., Lefort, P., and Pêcher, A., 1986, Geological research in the Nepal Himalayas: Annapurna-Manaslu-Ganesh Himal: Paris, Centre National de la Recherche Scientifique, 136 p.

Coleman, M.E., and Hodges, K.V., 1998, Contrasting Oligocene and Miocene thermal histories from the hanging wall and footwall of the South Tibetan detachment in the central Himalaya from $^{40}Ar/^{39}Ar$ thermochronology Marsyandi valley, central Nepal: Tectonics, v. 17, p. 726–740, doi:10.1029/98TC02777.

Cooper, F.J., Adams, B.A., Edwards, C.S., and Hodges, K.V., 2012, Large normal-sense displacement on the South Tibetan fault system in the eastern Himalaya: Geology, v. 40, no. 11, p. 971–974, doi:10.1130/G33318.1.

Cosca, M.A., Hunziker, J.C., Huon, S., and Masson, H., 1992, Radiometric age constraints on mineral growth, metamorphism, and tectonism of the Gummfluh Klippe, Briangonnais domain of the Prealpes, Switzerland: Contributions to Mineralogy and Petrology, v. 112, p. 439–449, doi:10.1007/BF00310776.

Cottle, J.M., Jessup, M.J., Newell, D.L., Searle, M.P., Law, R.D., and Horstwood, M.S.A., 2007, Structural insights into the early stages of exhumation along an orogen-scale detachment: The South Tibetan detachment system, Dzakaa Chu section, eastern Himalaya: Journal of Structural Geology, v. 29, p. 1781–1797, doi:10.1016/j.jsg.2007.08.007.

Cottle, J.M., Searle, M.P., Horstwood, M.S.A., and Waters, D., 2009, Timing of midcrustal metamorphism, melting, and deformation in the Mount Everest region of south Tibet revealed by U(-Th)-Pb geochronology: The Journal of Geology, v. 117, p. 643–664, doi:10.1086/605994.

Cottle, J.M., Waters, D.J., Riley, D., Beyssac, O., and Jessup, M.J., 2011, Metamorphic history of the South Tibetan detachment system, Mt. Everest region, revealed by RSCM thermometry and phase equilibria modeling: Journal of Metamorphic Geology, v. 29, p. 561–582, doi:10.1111/j.1525-1314.2011.00930.x.

Cottle, J.M., Searle, M.P., Jessup, M.J., Crowley, J.L., and Law, R.D., 2015, Rongbuk re-visited: Geochronology of leucogranites in the footwall of the South Tibetan detachment system, Everest region, southern Tibet: Lithos, v. 227, p. 94–106, doi:10.1016/j.lithos.2015.03.019.

Couch, E.L., and Grim, R.E., 1968, Boron fixation by illites: Clays and Clay Minerals, v. 16, p. 249–256, doi:10.1346/CCMN.1968.0160307.

Dunlap, W.J., 1997, Neocrystallization or cooling? $^{40}Ar/^{39}Ar$ ages of white micas from low-grade mylonites: Chemical Geology, v. 143, p. 181–203, doi:10.1016/S0009-2541(97)00113-7.

Dunlap, W.J., Teyssier, C., McDougall, I., and Baldwin, S., 1991, Ages of deformation from K/Ar and $^{40}Ar/^{39}Ar$ dating of white micas: Geology, v. 19, p. 1213–1216, doi:10.1130/0091-7613(1991)019<1213:AODFKA>2.3.CO;2.

Dutrow, B.L., and Henry, D.J., 2011, Tourmaline: A geologic DVD: Elements (Quebec), v. 7, p. 301–306, doi:10.2113/gselements.7.5.301.

Dutrow, B.L., and Henry, D.J., 2014, Tourmaline: The perfect accessory: Goldschmidt Abstracts, v. 2014, p. 610.

Dutrow, B.L., Foster, C.T., and Henry, D.J., 1999, Tourmaline-rich pseudomorphs in sillimanite zone metapelites: Demarcation of an infiltration front: The American Mineralogist, v. 84, p. 794–805.

Evans, M.A., and Dunne, W.M., 1991, Strain factorization and partitioning in the North Mountain thrust sheet, central Appalachians, USA: Journal of Structural Geology, v. 13, p. 21–35, doi:10.1016/0191-8141(91)90098-4.

Ferrill, D.A., and Groshong, R.H., Jr., 1993, Deformation conditions in the northern Subalpine Chain, France, estimated from deformation modes in coarse-grained limestone: Journal of Structural Geology, v. 15, p. 995–1006, doi:10.1016/0191-8141(93)90172-7.

Ferrill, D.A., Morris, P.A., Evans, M.A., Burkhard, M., Groshong, R.H., Jr., and Onasch, C.M., 2004, Calcite morphology: A low-temperature deformation geothermometer: Journal of Structural Geology, v. 26, p. 1521–1529, doi:10.1016/j.jsg.2003.11.028.

Gansser, A., 1964, Geology of the Himalayas: London, Interscience Publishers, John Wiley and Sons, 289 p.

Garzanti, E., 1999, Stratigraphy and sedimentary history of the Nepal Tethys Himalaya passive margin: Journal of Asian Earth Sciences, v. 17, p. 805–827, doi:10.1016/S1367-9120(99)00017-6.

Garzanti, E., Gorza, M., Martellini, L., and Nicora, A., 1994, Transition from diagenesis to metamorphism in the Paleozoic to Mesozoic succession of the Dolpo-Manang synclinorium and Thakkola fraben (Nepal Tethys Himalaya): Eclogae Geologicae Helvetiae, v. 87, p. 613–632.

Gébelin, A., Mulch, A., Teyssier, C., Jessup, M.J., Law, R.D., and Brunel, M., 2013, The Miocene elevation of Mount Everest: Geology, v. 41, p. 799–802, doi:10.1130/G34331.1.

Godin, L., 2003, Structural evolution of the Tethyan sedimentary sequence in the Annapurna area, central Nepal Himalaya: Journal of Asian Earth Sciences, v. 22, p. 307–328, doi:10.1016/S1367-9120(03)00066-X.

Godin, L., Brown, R.L., Hanmer, S., and Parrish, R., 1999a, Back folds in the core of the Himalayan orogen: An alternative interpretation: Geology, v. 27, p. 151–154, doi:10.1130/0091-7613(1999)027<0151:BFITCO>2.3.CO;2.

Godin, L., Brown, R.L., and Hanmer, S., 1999b, High strain zone in the hanging wall of the Annapurna detachment, central Nepal Himalaya, *in* MacFarlane, A., Sorkhabi, R.B., and Quade, J., eds., Himalaya and Tibet: Mountain Roots to Mountain Tops: Geological Society of America Special Paper 328, p. 199–210, doi:10.1130/0-8137-2328-0.199.

Godin, L., Parrish, R.R., Brown, R.L., and Hodges, K.V., 2001, Crustal thickening leading to exhumation of the Himalayan metamorphic core of central Nepal: Insight from U-Pb geochronology and $^{40}Ar/^{39}Ar$ thermochronology: Tectonics, v. 20, p. 729–747, doi:10.1029/2000TC001204.

Green, O.R., Searle, M.P., Corfield, R.I., and Corfield, R.M., 2008, Cretaceous–Tertiary carbonate platform evolution and the age of India–Asia collision along the Ladakh Himalaya (Northwest India): The Journal of Geology, v. 116, p. 331–353, doi:10.1086/588831.

Gregg, J.M., and Sibley, D.F., 1984, Epigenetic dolomitization and the origin of xenotopic dolomite texture: Journal of Sedimentary Petrology, v. 54, p. 908–931.

Grew, E.S., 1996, Borosilicates (exclusive of tourmaline) and boron in rock-forming minerals in metamorphic environments, *in* Grew, E.S., and Anovitz, L.M., eds., Boron: Mineralogy, Petrology and Geochemistry: Reviews in Mineralogy, v. 33, p. 388–502.

Guillot, S., LeFort, P., Pécher, A., Barman, M.R., and Aprahamian, J., 1995, Contact metamorphism and depth of emplacement of the Manaslu granite (central Nepal): Implications for Himalayan orogenesis: Tectonophysics, v. 241, p. 99–119, doi:10.1016/0040-1951(94)00144-X.

Gysin, M., and Lombard, A., 1959, Note sur la composition des roches métamorphiques et sédimentaires des sommets du Mont Everest-Lhotse (Himalaya): Archives des Sciences: Genéve, v. 12, p. 98–101.

Gysin, M., and Lombard, A., 1960, Observations complémentaires de pétrographie et de géologie dans le Massif du Mont Everest Lhotse: Eclogae Geologicae Helvetiae, v. 53, p. 189–204.

Haertel, M., Herwegh, M., and Pettke, T., 2013, Titanium-in-quartz thermometry on synkinematic quartz veins in a retrograde crustal-scale normal fault zone: Tectonophysics, v. 608, p. 468–481, doi:10.1016/j.tecto.2013.08.042.

Harper, D.A.T., Zhan, R., Stemmerik, L., Liu, J., Donovan, S.K., and Stouge, S., 2011, Ordovician on the roof of the world: Macro- and microfaunas from tropical carbonates in Tibet, *in* Gutiérrez-Marco, J.C., Rábano, I., and García-Bellido, D., eds., Ordovician of the World: Madrid, Spain, Instituto Geológico y Minero de España, p. 215–220.

Harrison, T.M., Ce'le'rier, J., Aikman, A.B., Hermann, J., and Heizler, M.T., 2009, Diffusion of ^{40}Ar in muscovite: Geochimica et Cosmochimica Acta, v. 73, p. 1039–1051, doi:10.1016/j.gca.2008.09.038.

Hawthorne, F.C., and Dirlam, D.M., 2011, Tourmaline the indicator mineral: From atomic arrangement to Viking navigation: Elements (Quebec), v. 7, p. 307–312, doi:10.2113/gselements.7.5.307.

Henry, D.J., and Dutrow, B.L., 1996, Metamorphic tourmaline and its petrologic applications, *in* Grew, E.S., and Anovitz, L.M., eds., Boron: Mineralogy, Petrology and Geochemistry: Reviews in Mineralogy, v. 33, p. 503–557.

Henry, D.J., and Dutrow, B.L., 2012, Tourmaline at diagenetic to low-grade metamorphic conditions: Its petrologic applicability: Lithos, v. 154, p. 16–32, doi:10.1016/j.lithos.2012.08.013.

Henry, D.J., and Guidotti, C.V., 2002, Titanium in biotite from metapelitic rocks: Temperature effects, crystal-chemical controls, and petrologic applications: The American Mineralogist, v. 87, p. 375–382, doi:10.2138/am-2002-0401.

Henry, D.J., Lu, G., and McCabe, C., 1994, Epigenetic tourmaline in sedimentary red-beds: An example from the Silurian Rose Hill Formation, Virginia: Canadian Mineralogist, v. 32, p. 599–605.

Henry, D.J., Guidotti, C.V., and Thomson, J.A., 2005, The Ti-saturation surface for low-to-medium pressure metapelitic biotites: Implications for geothermometry and Ti-substitution mechanisms: The American Mineralogist, v. 90, p. 316–328, doi:10.2138/am.2005.1498.

Hirth, G., and Tullis, J., 1992, Dislocation creep regimes in quartz aggregates: Journal of Structural Geology, v. 14, p. 145–159, doi:10.1016/0191-8141(92)90053-Y.

Hodges, K.V., 2000, Tectonics of the Himalaya and southern Tibet from two perspectives: Geological Society of America Bulletin, v. 112, p. 324–350.

Hodges, K.V., Hubbard, M.S., and Silverberg, D.S., 1988, Metamorphic constraints on the thermal evolution of the central Himalayan orogen: Philosophical Transactions of the Royal Society of London, v. 326, p. 257–280, doi:10.1098/rsta.1988.0087.

Hodges, K.V., Parrish, R.R., Housh, T.B., Lux, D.R., Burchfiel, B.C., Royden, L.H., and Chen, Z., 1992, Simultaneous Miocene extension and shortening in the Himalayan orogen: Science, v. 258, p. 1466–1470, doi:10.1126/science.258.5087.1466.

Holyoke, C.W., and Kronenberg, A.K., 2010, Accurate differential stress measurement using the molten salt cell and solid salt assemblies in the Griggs apparatus with application to strength piezometers and rheology: Tectonophysics, v. 494, p. 17–31, doi:10.1016/j.tecto.2010.08.001.

Hubbert, M.K., and Rubey, W.W., 1959, Role of fluid pressure in the mechanics of overthrust faulting: Geological Society of America Bulletin, v. 70, p. 115–166, doi:10.1130/0016-7606(1959)70[115:ROFPIM]2.0.CO;2.

Jessup, M.J., Law, R.D., Searle, M.P., and Hubbard, M.S., 2006, Structural evolution and vorticity of flow during extrusion and exhumation of the Greater Himalayan Slab, Mount Everest massif, Tibet/Nepal: Implications for orogen-scale flow partitioning, *in* Law, R.D., Searle, M.P., and Godin, L., eds., Channel Flow, Ductile Extrusion and Exhumation in Continental Collision Zones: Geological Society of London Special Publication 268, p. 379–413, doi:10.1144/GSL.SP.2006.268.01.18.

Jessup, M.J., Cottle, J.M., Searle, M.P., Law, R.D., Newell, D.L., Tracy, R.J., and Waters, D.J., 2008, *P-T-t-D* paths of Everest Series schist, Nepal: Journal of Metamorphic Geology, v. 26, p. 717–739, doi:10.1111/j.1525-1314.2008.00784.x.

Kellett, D.A., and Godin, L., 2009, Pre-Miocene deformation of the Himalayan superstructure, central Nepal: Journal of the Geological Society of London, v. 166, p. 261–275, doi:10.1144/0016-76492008-097.

Kirschner, D.L., Cosca, M.A., Masson, H., and Hunziker, J.C., 1996, Staircase $^{40}Ar/^{39}Ar$ spectra of fine-grained white mica: Timing and duration of deformation and empirical constraints on argon diffusion: Geology, v. 24, no. 8, p. 747–750, doi:10.1130/0091-7613(1996)024<0747:SAASOF>2.3.CO;2.

Law, R.D., Searle, M.P., and Simpson, R.L., 2004, Strain, deformation temperatures and vorticity of flow at the top of the Greater Himalayan Slab, Everest Massif, Tibet: Journal of the Geological Society of London, v. 161, p. 305–320, doi:10.1144/0016-764903-047.

Law, R.D., Jessup, M.J., Searle, M.P., Francsis, M.K., Waters, D.J., and Cottle, J.M., 2011, Telescoping of isotherms beneath the South Tibetan detachment system, Mount Everest Massif: Journal of Structural Geology, v. 33, p. 1569–1594, doi:10.1016/j.jsg.2011.09.004.

Leloup, P.H., Mahéo, G., Arnaud, N., Kali, E., Boutonnet, E., Liu, D., Xiahan, L., Haibing, L., 2010, The South Tibetan detachment shear zone in the Dinggye area: Time constraints on extrusion models of the Himalayas: Earth and Planetary Science Letters, v. 292, p. 1–16, doi:10.1016/j.epsl.2009.12.035.

Lerman, A., 1966, Boron in clays and estimation of palaeosalinities: Sedimentology v. 6, p. 267–286.

Li, S., Wang, S., Chen, Y., Liu, D., Qiu, J., Zhou, H., and Zhang, Z., 1994, Excess argon in phengite from eclogite: Evidence from dating of eclogite minerals by Sm-Nd, Rb-Sr and $^{40}Ar/^{39}Ar$ methods: Chemical Geology, v. 112, p. 343–350, doi:10.1016/0009-2541(94)90033-7.

Lombardo, B., Pertusati, P., and Borgi, S., 1993, Geology and tectonomagmatic evolution of the eastern Himalaya along the Chomolungma-Makalu transect, *in* Treloar, P.J., and Searle, M.P., eds., Himalayan Tectonics: Geological Society of London Special Publication 74, p. 341–355, doi:10.1144/GSL.SP.1993.074.01.23.

London, D., 1999, Stability of tourmaline in peraluminous granite systems: The boron cycle from anatexis to hydrothermal aureoles: European Journal of Mineralogy, v. 11, p. 253–262, doi:10.1127/ejm/11/2/0253.

London, D., Morgan, G.B., VI, and Wolf, M.B., 1996, Boron in granitic rocks and their contact aureoles, *in* Grew, E.S., and Anovitz, L.M., eds., Boron: Mineralogy, Petrology and Geochemistry: Reviews in Mineralogy, v. 33, p. 299–330.

Massonne, H.J., and Schreyer, W., 1987, Phengite geobarometry based on the limiting assemblage with K-feldspar, phlogopite, and quartz: Contributions to Mineralogy and Petrology, v. 96, p. 212–224, doi:10.1007/BF00375235.

McDougall, I., and Harrison, M.T., 1999, Geochronology and Thermochronology by the $^{40}Ar/^{39}Ar$ Method, Volume 2: New York, Oxford University Press, 269 p.

Morgan, G.B.V.I., and London, D., 1987, Behavior of boron and tourmaline stability in granitic systems: Geologic Society of America Abstracts Programs, v. 19, no. 7, p. 777–778.

Mulch, A., and Cosca, M.A., 2004, Recrystallization or cooling ages: In situ UV-laser $^{40}Ar/^{39}Ar$ geochronology of muscovite in mylonitic rocks: Journal of the Geological Society of London, v. 161, p. 573–582, doi:10.1144/0016-764903-110.

Mulch, A., Cosca, M.A., and Handy, M.R., 2002, In-situ UV-laser $^{40}Ar/^{39}Ar$ geochronology of a micaceous mylonite: An example of defect-enhanced argon loss: Contributions to Mineralogy and Petrology, v. 142, p. 738–752, doi:10.1007/s00410-001-0325-6.

Murphy, M.A., and Harrison, T.M., 1999, Relationship between leucogranites and the Qomolangma detachment in the Rongbuk Valley, south Tibet: Geology, v. 27, p. 831–834, doi:10.1130/0091-7613(1999)027<0831:RBLATQ>2.3.CO;2.

Murphy, M.A., and Yin, A., 2003, Structural evolution and sequence of thrusting in the Tethyan fold-thrust belt and Indus-Yalu suture zone, southwest Tibet: Geological Society of America Bulletin, v. 115, p. 21–34, doi:10.1130/0016-7606(2003)115<0021:SEASOT>2.0.CO;2.

Myrow, P.M., Hughes, N.C., Searle, M.P., Fanning, C.M., Peng, S.C., and Parcha, S.K., 2009, Stratigraphic correlation of Cambrian–Ordovician deposits along the Himalaya: Implications for the age and nature of rocks in the Mount Everest region: Geological Society of America Bulletin, v. 121, p. 323–332, doi:10.1130/B26384.1.

Odell, N.E., 1925, Observations on the rocks and glaciers of Mount Everest: The Geographical Journal, v. 66, p. 289–313, doi:10.2307/1782942.

Odell, N.E., 1967, Highest fossils in the world: Geological Magazine, v. 104, p. 73–76, doi:10.1017/S0016756800040437.

Passchier, C.W., and Trouw, R.A.J., 2005, Microtectonics: Berlin, Springer-Verlag 366 p.

Pêcher, A., 1989, The metamorphism in the central Himalaya: Journal of Metamorphic Geology, v. 7, p. 31–41, doi:10.1111/j.1525-1314.1989.tb00573.x.

Pognante, U., and Benna, P., 1993, Metamorphic zonation, migmatization and leucogranites along the Everest transect of eastern Nepal and Tibet: Record of an exhumation history, *in* Treloar, P.J., and Searle, M.P., eds., Himalayan Tectonics: Geological Society of London Special Publication 74, p. 323–340, doi:10.1144/GSL.SP.1993.074.01.22.

Prince, C., Harris, N., and Vance, D., 2001, Fluid-enhanced melting during prograde metamorphism: Journal of the Geological Society of London, v. 158, no. 2, p. 233–241, doi:10.1144/jgs.158.2.233.

Radke, B.M., and Mathis, R.L., 1980, On the formation and occurrence of saddle dolomite: Journal of Sedimentary Petrology, v. 50, p. 1149–1168.

Rosenberg, P.E., and Foit, F.F., Jr., 2006, Magnesiofoititе from the uranium deposits of the Athabasca Basin, Saskatchewan, Canada: Canadian Mineralogist, v. 44, p. 959–965, doi:10.2113/gscanmin.44.4.959.

Rusk, B.G., Reed, M.H., Dilles, J.H., and Kent, A.J.R., 2006, Intensity of quartz cathodoluminescence and trace-element content in quartz from the porphyry copper deposit at Butte, Montana: The American Mineralogist, v. 91, p. 1300–1312, doi:10.2138/am.2006.1984.

Rutter, E.H., 1995, Experimental study of the influence of stress, temperature, and strain on the dynamic recrystallization of Carrara marble: Journal of Geophysical Research, v. 100, p. 24,651–24,663, doi:10.1029/95JB02500.

Sakai, H., 1997, Detachment fault below the summit of Mt. Everest and its tectonic significance in the Himalayan orogeny: Journal of the Geological Society of Japan, v. 103, no. 3, p. 240–252, doi:10.5575/geosoc.103.240.

Sakai, H., Sawada, M., Takigami, Y., Orihashi, Y., Danhara, T., Iwano, H., Kuwahara, Y., Dong, Q., Cai, H., and Li, J., 2005, Geology of the summit limestone of Mount Qomolangma (Everest) and cooling of the Yellow Band under the Qomolangma detachment: The Island Arc, v. 14, p. 297–310, doi:10.1111/j.1440-1738.2005.00499.x.

Scaillet, B., France-Lanord, C., and LeFort, P., 1990, Badrinath-Gangotri plutons (Garhwal, India): Petrological and geochemical evidence for fractionation processes in a high Himalayan leucogranite: Journal of Volcanology and Geothermal Research, v. 44, p. 163–188, doi:10.1016/0377-0273(90)90017-A.

Scaillet, B., Holtz, F., Pichavant, M., and Schmidt, M., 1996, Viscosity of Himalayan leucogranites: Implications for mechanisms of granitic magma ascent: Journal of Geophysical Research–Solid Earth, v. 101, p. 27,691–27,699, doi:10.1029/96JB01631.

Schenk, O., Urai, J.L., and Evens, B., 2005, The effect of water on recrystallization behavior and grain boundary morphology in calcite—Observations of natural marble mylonites: Journal of Structural Geology, v. 27, p. 1856–1872, doi:10.1016/j.jsg.2005.05.015.

Schmid, S.M., Paterson, M.S., and Boland, J.N., 1980, High temperature flow and dynamic recrystallization in Carrara marble: Tectonophysics, v. 65, p. 245–280, doi:10.1016/0040-1951(80)90077-3.

Schneider, C., and Masch, L., 1993, The metamorphism of the Tibetan Series from the Manang area, Marsyandi Valley, Central Nepal, *in* Treloar, P.J., and Searle, M.P. eds., Himalayan Tectonics: Geological Society of London Special Publication 74, p. 357–374, doi:10.1144/GSL.SP.1993.074.01.24.

Scoffin, T.P., 1987, Carbonate Sediments and Rocks: Glasgow, Blackie, 274 p.

Searle, M.P., 1999a, Extensional and compressional faults in the Everest-Lhotse massif, Khumbu Himalaya, Nepal: Journal of the Geological Society of London, v. 156, p. 227–240, doi:10.1144/gsjgs.156.2.0227.

Searle, M.P., 1999b, Emplacement of Himalayan leucogranites by magma injection along giant sill complexes: Examples from the Cho Oyu, Gyachung Kang and Everest leucogranites (Nepal Himalaya): Journal of Asian Earth Sciences, v. 17, p. 773–783, doi:10.1016/S1367-9120(99)00020-6.

Searle, M.P., 2003, Geological Map of the Mount Everest—Makalu Region, Nepal–South Tibet Himalaya (2nd edition 2007): Oxford, UK, Department of Earth Sciences, Oxford University, scale 1:100,000, 1 sheet.

Searle, M.P., 2013, Crustal melting, ductile flow, and deformation in mountain belts: Cause and effect relationships: Lithosphere (in press), doi:10.1130/RF.L006.1.

Searle, M.P., and Godin, L., 2003, The South Tibetan detachment and the Manaslu leucogranite: A structural reinterpretation and restoration of the Annapurna-Manaslu Himalaya, Nepal: The Journal of Geology, v. 111, p. 505–523, doi:10.1086/376763.

Searle, M.P., Simpson, R.L., Law, R.D., Waters, D.J., and Parrish, R.R., 2002, Quantifying displacement on the South Tibetan detachment normal fault, Everest massif, and the timing of crustal thickening and uplift in the Himalaya and South Tibet: Journal of the Nepal Geological Society, v. 160, p. 1–6.

Searle, M.P., Simpson, R.L., Law, R.D., Parrish, R.R., and Waters, D.J., 2003, The structural geometry, metamorphic and magmatic evolution of the Everest massif, High Himalaya of Nepal–South Tibet: Journal of the Geological Society of London, v. 160, p. 345–366, doi:10.1144/0016-764902-126.

Searle, M.P., Law, R.D., and Jessup, M.J., 2006, Crustal structure, restoration and evolution of the Greater Himalaya in Nepal–South Tibet: Implications for channel flow and ductile extrusion of the middle crust, *in* Law, R.D., Searle, M.P., and Godin, L., eds., Channel Flow, Ductile Extrusion and Exhumation in Continental Collision Zones: Geological Society of London Special Publication 268, p. 355–378, doi:10.1144/GSL.SP.2006.268.01.17.

Searle, M.P., Cottle, J.M., Streule, M.J., and Waters, D.J., 2009, Crustal melt granites and migmatites along the Himalaya: Melt source, segregation, transport and granite emplacement mechanisms: Earth and Environmental Science Transactions of the Royal Society of Edinburgh, v. 100, p. 219–233, doi:10.1017/S175569100901617X.

Sibley, D.F., and Gregg, J.M., 1987, Classification of dolomite rock textures: Journal of Sedimentary Petrology, v. 57, p. 967–975.

Simpson, R.L., Parrish, R.R., Searle, M.P., and Waters, D.J., 2000, Two episodes of monazite crystallization during metamorphism and crustal melting in the Everest region of the Nepalese Himalaya: Geology, v. 28, p. 403–406, doi:10.1130/0091-7613(2000)28<403:TEOMCD>2.0.CO;2.

Spear, F.S., 1993, Metamorphic Phase Equilibria and Pressure-Temperature-Time Paths: Mineralogical Society of America Monograph 1, p. 799.

Srivastava, N.K., and Schnitzer, W.A., 1976, Authigenic minerals in the Precambrian sedimentary rocks of the Chattisgarh System (central India): Neues Jahrbuch für Mineralogie, v. 126, p. 221–230.

Stipp, M., and Tullis, J., 2003, The recrystallized grain size piezometer for quartz: Geophysical Research Letters, v. 30, p. 2088, doi:10.1029/2003GL018444.

Stipp, M., Stünitz, H., Heilbronner, R., and Schmid, S.M., 2002a, The eastern Tonale fault zone: A "natural laboratory" for crystal plastic deformation of quartz over a temperature range from 250 to 700 °C: Journal of Structural Geology, v. 24, p. 1861–1884, doi:10.1016/S0191-8141(02)00035-4.

Stipp, M., Stunitz, H., Heilbronner, R., and Schmid, S., 2002b, Dynamic recrystallization of quartz: Correlation between natural and experimental conditions, *in* De Meer, S., Drury, M.R., De Bresser, J.H.P., and Pennock, G.M., eds., Deformation Mechanisms, Rheology and Tectonics: Current Status and Future Perspectives: Geological Society of London Special Publication 200, p. 171–190, doi:10.1144/GSL.SP.2001.200.01.11.

Streule, M.J., Carter, A., Searle, M.P., and Cottle, J.M., 2012, Constraints on brittle field exhumation of the Everest-Makalu section of the Greater Himalayan Sequence: Implications for models of crustal flow: Tectonics, v. 31, p. TC3010, doi:10.1029/2011TC003062.

Thomas, J.B., Watson, E.B., Spear, F.S., Shemella, F.S., Nayak, S.K., and Lanzirotti, A., 2010, TitaniQ under pressure: The effect of pressure and temperature on the solubility of Ti in quartz: Contributions to Mineralogy and Petrology, v. 160, p. 743–759, doi:10.1007/s00410-010-0505-3.

Thompson, J.B., Jr., 1959, Local equilibrium in metasomatic processes, *in* Abelson, P.H., ed., Researches in Geochemistry: New York, John Wiley, p. 427–457.

Torsvik, T.H., Paulson, T.S., Hughes, N.C., Myrow, P.M., and Ganerød, M., 2009, The Tethyan Himalaya: Palaeogeographical and tectonic constraints from Ordovician palaeomagnetic data: Journal of the Geological Society of London, v. 166, p. 679–687, doi:10.1144/0016-76492008-123.

van Hinsberg, V.J., Henry, D.J., and Dutrow, B.L., 2011a, Tourmaline as a petrologic forensic mineral: A unique recorder of its geologic past: Elements (Quebec), v. 7, p. 327–332, doi:10.2113/gselements.7.5.327.

van Hinsberg, V.J., Henry, D.J., and Marschall, H.R., 2011b, Tourmaline: An ideal indicator of its host environment: Canadian Mineralogist, v. 49, p. 1–16, doi:10.3749/canmin.49.1.1.

Vannay, J.C., and Hodges, K.V., 1996, Tectonomorphic evolution of the Himalayan metamorphic core between the Annapurna and Dhaulagiri, central Nepal: Journal of Metamorphic Geology, v. 14, p. 635–656, doi:10.1046/j.1525-1314.1996.00426.x.

Velde, B., 1967, Si^{+4} content of natural phengites: Contributions to Mineralogy and Petrology, v. 14, p. 250–258, doi:10.1007/BF00376643.

Viskupic, K., and Hodges, K.V., 2001, Monazite-xenotime thermochronometry: Methodology and an example from the Nepalese Himalaya: Contributions to Mineralogy and Petrology, v. 141, p. 233–247, doi:10.1007/s004100100239.

Viskupic, K., Hodges, K.V., and Bowring, S.A., 2005, Timescales of melt generation and the thermal evolution of the Himalayan metamorphic core, Everest region, eastern Nepal: Contributions to Mineralogy and Petrology, v. 149, p. 1–21, doi:10.1007/s00410-004-0628-5.

Wager, L.R., 1934, A review of the geology and some new observations, *in* Ruttledge, H., eds., Everest 1933: London, Hodder & Stoughton, p. 312–336.

Walther, J.V., 1990, Fluid dynamics during progressive regional metamorphism, *in* Bredehoft, J.D., and Norton, D.L., eds., The Role of Fluids in Crustal Processes: Washington, D.C., National Academy of Sciences, p. 64–71.

Walther, J.V., and Orville, P.M., 1980, Rates of metamorphism and volatile production and transport in regional metamorphism: Geological Society of America Abstracts Programs, v. 12, no. 7, p. 544.

Walther, J.V., and Orville, P.M., 1982, Volatile production and transport in regional metamorphism: Contributions to Mineralogy and Petrology, v. 79, p. 252–257, doi:10.1007/BF00371516.

Wark, D.A., and Watson, E.B., 2006, The TitaniQ: A titanium-in-quartz geothermometer: Contributions to Mineralogy and Petrology, v. 152, p. 743–754, doi:10.1007/s00410-006-0132-1.

Waters, D.J., Law, R.D., and Searle, M.P., 2006, Metamorphic evolution of the upper parts of the Greater Himalayan Slab, Everest area, from the 1933 sample collection of L.R. Wager: Journal of Asian Earth Sciences, v. 26, p. 168.

Weisbrod, A., Polak, C., and Roy, D., 1986, Experimental study of tourmaline solubility in the system Na-Mg-Al-Si-B-O-H: Applications to the boron content of natural hydrothermal fluids and tourmalinization processes: International Symposium on Experimental Mineralogy Abstracts, v. 1, p. 140–141.

Yardley, B.W.D., 1997, Evolution of fluids through the metamorphic cycle, *in* Jamveit, B., and Yardley, B.W.D., eds., Fluid Flow and Transport in Rocks: London, Chapman-Hall, p. 99–121, doi:10.1007/978-94-009-1533-6_6.

Yin, A., 2006, Cenozoic tectonic evolution of the Himalayan orogen as constrained by along-strike variation of structural geometry, exhumation history, and foreland sedimentation: Earth-Science Reviews, v. 76, p. 1–131, doi:10.1016/j.earscirev.2005.05.004.

Yin, C.H., and Kuo, S.T., 1978, Stratigraphy of the Mount Jolmo Lungma and its north slope: Scientia Sinica, v. 21, p. 629–644.

Zhu, W.P., and Wei, C.J., 2007, Thermodynamic modelling of the phengite geobarometry: Science in China Press, v. 50, p. 1033–1039, doi:10.1007/s11430-007-0046-4.

MANUSCRIPT RECEIVED 22 JUNE 2015
REVISED MANUSCRIPT RECEIVED 26 SEPTEMBER 2015
MANUSCRIPT ACCEPTED 19 OCTOBER 2015

Printed in the USA